



Estimation of superficial snow specific surface area from spectral albedo time-series at Dome C, Antarctica

G. Picard^{1,2}, Q. Libois¹, L. Arnaud¹, G. Verin¹, and M. Dumont³

¹UJF – Grenoble 1 / CNRS, Laboratoire de Glaciologie et Géophysique de l'Environnement (LGGE) UMR 5183, Grenoble, F-38041, France

²ACE CRC, University of Tasmania, Private Bag 80, Hobart, TAS 7001, Australia

³Météo-France – CNRS, CNRM – GAME UMR 3589, Centre d'Études de la Neige, Grenoble, France

Correspondence to: Ghislain Picard (ghislain.picard@ujf-grenoble.fr)

Abstract. Spectral albedo of the snow surface in the visible/near-infrared range has been measured for 3 years by an automatic spectral radiometer installed at Dome C (75°S, 123°E) in Antarctica in order to retrieve specific surface area (SSA) of superficial snow. This study focuses on the uncertainties of the SSA retrieval due to the instrument deficiencies and issues related to data processing. We find that when the solar zenith angle is high, the main source of error is the imperfect angular response of the light collectors. This imperfection introduces a small spurious wavelength-dependent trend in the albedo spectra which greatly affects the SSA retrieval. By modeling this effect, we show that for typical snow and illumination conditions encountered at Dome C, retrieving SSA with an accuracy better than 15% (our target), requires the slope of this trend not to exceed 2% between 400 and 1100 nm. Such a small slope can be achieved only by i) careful design of the collectors, ii) an ad hoc correction of the spectra using the actual measured angular response of the collectors, and iii) for solar zenith angles less than 75°. The comparison of the retrieved SSA with independent measurements made with an optical device operating at 1310 nm confirms the presence of a sharp and recurrent vertical gradient of SSA in the uppermost centimeter at Dome C, which challenges the assessment of the absolute accuracy from independent measurements. Nevertheless, with three-fold variations of SSA during the summer seasons, we conclude that the retrieved SSA is accurate enough to provide a detailed picture of the October-March evolution of the surface snow at Dome C.

1 Introduction

The summer surface energy budget on the ice sheets is largely controlled by the absorption of solar energy by snow (Van As et al., 2005; Ettema et al., 2010). The latter is determined by the downward irradiance reaching the surface and by snow albedo. With solar irradiance of several hundreds of W m^{-2} during daylight, a persistent change of 1% of the albedo represents an energy comparable with the external forcing caused by CO_2 concentration increase since pre-industrial time (1.82 W m^{-2} , Myhre et al., 2009). While planetary albedo change is not expected to exceed a tenth of this value (Myhre et al., 2009), local changes can be much larger owing to the dependence of snow albedo on multiple factors including snow grain size and shape, surface roughness, snow depth, and the amount of light-absorbing impurities such as black carbon, dust and biological pigments (Warren and Wiscombe, 1980; Warren et al., 1998; Aoki et al., 2000; Dumont et al., 2010; Zhuravleva and Kokhanovsky, 2011;



Stibal et al., 2012; Goelles et al., 2015, e.g.). These factors vary in space and time depending on the atmospheric conditions and are controlled by numerous processes giving rise to complex snow-albedo feedback loops between the snow cover and the atmosphere (Curry et al., 1995; Qu and Hall, 2007; Picard et al., 2012). In Antarctica, snow grain size is the main factor controlling the albedo along with the illumination conditions (solar zenith angle and cloud cover) and surface roughness while the impurity content is usually low (Warren et al., 2006). Investigating the feedback loops thus requires long-term and accurate observations of albedo and snow properties.

Nevertheless, albedo measurements in Antarctica are scarce and subject to artifacts. Only a few Baseline Surface Radiation Network (BSRN) stations and some automatic weather stations deployed by the Institute of Marine and Atmospheric research (Utrecht University) provide time series of broadband albedo measured using upward and downward looking pyranometers. These sensors are subject to many artifacts such as imperfect response at high solar zenith angle, leveling and frost, which are difficult to correct (van den Broeke et al., 2004; Nicolaus et al., 2010; Bogren et al., 2015). Retrieving broadband albedo from remote sensing is not a straightforward alternative. It requires atmospheric correction, spectra extrapolation from a limited number of spectral bands, and angular extrapolation of the bi-conical measurements to get hemispherical surface reflectance (Stroeve et al., 2006). The latter is challenging because the bi-directional reflectance of snow is much more sensitive to grain shape (Dumont et al., 2010) and surface roughness (Kuchiki et al., 2011) than hemispherical reflectance (i.e. albedo), thus introducing extra uncertain variables that need to be estimated somehow. Moreover, satellite data can not be used under cloudy conditions or when the sun zenith angle is too high (Wang and Zender, 2010; Schaaf et al., 2011). Even with a few overpasses of the satellites per day, the time-series are discontinuous and snowfalls, which are periods of great albedo change, are systematically missed.

Measuring snow grain size is difficult as well. Estimating the maximal extent of the dominant crystals using hand-lens or binocular is the most widely used technique to measure grain size (Fierz et al., 2009; Aoki et al., 2000; Pirazzini et al., 2015). However, not only it is known to be imprecise and operator-dependent, but it can not be automated for unmanned monitoring of grain size evolution. Recent advances in field measurement of the specific surface area (the surface area of the air-ice interface per unit of mass of snow) – which is equivalent to the optical radius commonly used in remote sensing (Grenfell and Warren, 1999; Nolin and Dozier, 2000; Jin et al., 2008) – offer an attractive alternative. Examples of instruments and methods include contact spectroscopy (Painter et al., 2007), near-infrared photography (Matzl and Schneebeli, 2006), DUFISSS and IceCUBE (Gallet et al., 2009) and POSSSUM and ASSSAP (Arnaud et al., 2011). These techniques being based on optical measurements of the snow reflectance in the near or short wave infrared, it is arguable whether they provide data more related to albedo or a proper geometrical metric of the snow micro-structure. Several theoretical studies have indeed shown the significant influence of the snow crystal shape on the albedo (Macke and Mishchenko, 1996; Neshyba et al., 2003; Kokhanovsky and Zege, 2004; Picard et al., 2009) and on the e-folding depth (Libois et al., 2013) but no clear experimental evidence of this effect has been given yet for snow on the ground (Gallet et al., 2009; Libois et al., 2014b). In fact, these optical techniques have been shown to be accurate within 15% when compared with independent measurements using methane adsorption or micro-computed tomography techniques (Matzl and Schneebeli, 2006; Domine et al., 2006; Gallet et al., 2009). This accuracy is sufficient to achieve a 1% accuracy of broadband albedo (Gardner and Sharp, 2010) which is considered to be adequate for climate study



(Bogren et al., 2015). Intensive campaigns of SSA measurements have provided new insight of the snow metamorphism in the Alps and in Antarctica over seasons and have allowed refined evaluation of detailed snow model predictions (Picard et al., 2012; Morin et al., 2013; Roy et al., 2013; Libois et al., 2015). However, these techniques still require an operator which is often a limitation, particularly in the Antarctic. Optical satellite remote sensing has been used to retrieve optical radius (e.g. Nolin and Dozier, 2000; Painter et al., 2009; Negi et al., 2011; Mary et al., 2013) in particular in Antarctica (Scambos et al., 2007; Jin et al., 2008). Mary et al. (2013) and Tanikawa et al. (2015) give an overview of the numerous existing algorithms. Obtaining grain size on a large spatial extent and for many years is of great interest, but attaining an accuracy similar to that of field techniques requires to overcome several additional defects that are specific to space-borne sensors and are in fact very similar to those faced for albedo retrieval. Microwave remote sensing is not subject to these issues but as far as albedo study is concerned, only the highest available frequencies could be able to provide superficial grain size (Picard et al., 2012). However, the technique proposed by Picard et al. (2012) is specific in many ways to the conditions of the Antarctic Plateau and requires additional assumptions about the density and temperature of superficial snow compared to the optic domain.

Ground-based observation of spectral albedo has several advantages compared to broadband measurement: it can provide a finer understanding of the albedo variation and can be used to estimate SSA using similar principles to those used in remote sensing and by the optical techniques mentioned above. It is also easier to assess the data quality or develop corrections by exploiting the spectral signature. Many spectral albedo measurements have been conducted in Antarctica (e.g. Grenfell et al., 1994; Hudson et al., 2006; Hudson and Warren, 2007; Marks et al., 2015; Pirazzini et al., 2015) but they were limited to short term campaigns and the temporal evolution was not the priority. Long-term monitoring of spectral albedo requires fully automated instruments with a good robustness to cop with the Antarctic conditions. With the advent of cheaper and compact spectrometers free of mechanical parts (Kantzas et al., 2009; Nicolaus et al., 2010), operating such instruments in Antarctic conditions is becoming easier.

The objective of the present study is to describe the automatic spectral radiometer that we developed and installed at Dome C and the data processing developed to estimate time-series of spectral albedo and SSA from the raw measurements. We particularly focus on the uncertainties of the estimated albedo and SSA. For this, we analyze the improvement of the quality through the successive processing steps. We discuss the results in the light of a SSA target uncertainty of 15%, as claimed to be reached by manual devices (near-infrared photography, DUFISSS, POSSSUM) and considering it is difficult to perform better than those man-operated tools. Theoretical modeling of the imperfections of the instrument are used to help in this analysis and also to provide quantitative recommendations for the design of future spectral radiometers. At last the representativeness of the estimated SSA is explored by comparing the estimates with independent measurements and by using radiative transfer simulations. The geophysical interpretation of the 3-year long SSA time-series obtained with our instrument and its comparison to snow model simulations are addressed in Libois et al. (2015).

Section 2 describes the instrument, the processing and method to retrieve SSA. Results are presented in section 3 and discussion and conclusion is provided in the last section.



2 Materials and method

The spectral albedo of the surface is measured at Dome C (75°S, 123°E) with a home-made instrument presented in the first section. The second section details the construction and characterization of the light collectors (or fore optics) that are critical to achieve high quality measurements. The third section presents the data processing steps to derive spectral albedo from raw data and the last section addresses the retrieval of the surface specific area of superficial snow.

2.1 Automatic measurements of spectral albedo

We designed and assembled an instrument composed of several commercial and home-made components to automatically measure spectral albedo. The main specifications driving the design was the robustness to work in the Dome C harsh environment for several years and the ability to acquire not only albedo (incident and reflected radiation) but also the radiation within the snow at several levels (not used in this study), thus requiring a spectrometer with many inputs. The instrument is named Autosolexs (Automatic SOLar Extinction in Snow) because of the latter application.

Figure 1 shows pictures of the visible above-ground part of the system which comprises two heads for albedo measurements at about 2 m above the surface. This height has decreased at an averaged rate of about 10 cm per year since the installation. Each head is equipped with two light collectors looking upward and downward. The collected radiations are transmitted by 6-m long fiber optics (core diameter of 400 μm) to the rest of the device that is buried under the snow. Neither electronic nor fragile parts are above-ground.

The instrument scheme is depicted in Fig. 2. The fibers coming from the heads are directly connected to the inputs of a 16-to-1 optical switch (FiberSwitch mol 1 \times 16 19" 2 HU by Leoni). Using a mechanic-optical module driven by a digital interface, it links in a few milliseconds one of the 16 inputs to the output with a reproducibility better than 0.03 dB according to the manufacturer. This corresponds to about 0.7% uncertainty for the irradiance which in the worse case translates to 1.4% for the albedo. The output of the switch is connected to a splitter 1-to-2 that transmits radiation to two spectrometers (MAYA PRO, Ocean Optics). One covers the visible near infrared and the second one is dedicated to the ultraviolet. Only the former is used in this study. It gives signal above the noise level in the range 350 - 1050 nm with an effective spectral resolution of 3 nm. One of the inputs of the optical switch is obstructed so it measures dark conditions that are used to correct the offset present in the spectrometer acquisitions. The instrument container is thermalized at $+10\pm 2^\circ\text{C}$ which is necessary for the good operation and stability of the spectrometers.

An embedded computer controls the optical switch, the spectrometers and schedules the acquisition. Every 12 min, a complete sequence of measurements is performed in the following order: head 1 (incident and then reflected channels), head 2 (incident and then reflected channels), buried fibers, heads 1 and 2 again, and at last dark. Each measurement takes 10-20 seconds. An automatic camera is connected to the computer to take one picture per sequence like those shown in Fig. 1. This provides qualitative but very useful information on the state of the snow surface and the presence of frost on the light collectors. The system is connected to the power supply of the Concordia station – the power consumption is typically around 50 W – and to the network to send data in near-real time.



2.2 Design and characterization of the light collectors

The light collectors are an important component. Albedo – or more rigorously bi-hemispherical reflectance (Schaepman-Strub et al., 2006) – is the ratio of the upwelling and downwelling fluxes, and the flux is the energy (per unit of surface, of time and of wavelength) crossing an horizontal surface. To measure flux, the collector must have a so-called cosine response so that the energy coming with an oblique direction is weighted by the cosine of the zenith angle (Grenfell et al., 1994; Morrow et al., 2000).

In principle, a flat surface which transmits a constant proportion of the incident beam whatever its direction acts as a perfect collector. For this reason, collectors are often made of a flat disk of highly diffusing material like sintered teflon grains. Nevertheless, teflon grains, like snow grains, have a strong forward scattering behavior so that flat collectors are more reflective at grazing angles than for the normal incidence. As a result, they transmit less at grazing angles than what is required for a perfect cosine response. When the sun is low on the horizon and in clear sky conditions, the downwelling irradiance has a strong and grazing direct component and the upward-looking collector thus tends to under-estimate the incoming flux. In contrast, the irradiance reflected back by the snow is always more diffuse and the down-looking collector is therefore almost not affected by this issue. This differential behavior usually results in an over-estimation of the albedo which increases with the solar zenith angle and depends on the direct/diffuse ratio of the sky.

This problem is particularly serious because it strongly depends on the wavelength. This arises because both the light collector materials and the sky depend on scattering intensity which usually decreases with longer wavelengths. Hence, the collector angular response changes with the wavelength from a near-ideal cosine response in the blue part of the solar spectrum to a nadir peaked response at longer wavelengths (Grenfell et al., 1994). This effect is enhanced by the decrease of the direct/diffuse component ratio of the downwelling irradiance under clear-sky conditions, with the wavelength. The albedo is therefore subject to chromatic aberration (wavelength dependent response) that depends on the sun elevation, cloudiness, and other factors affecting the spectral and angular characteristics of the illumination.

To address this difficulty, we took a two-fold strategy consisting of building and optimizing our own collectors, and applying an *ad hoc* correction to remove the residual imperfections using the actual response of the collectors.

Our collectors are made of a bumped surface cap (Figure 3) following design proposed by Bernhard and Seckmeyer (1997) to compensate for the reduced transmission at grazing angles. However, a side-effect of this design is that the light transmitted through the cap is not emerging symmetrically with respect to the collector axis (shown in Figure 3) but is more intense in the azimuthal direction of the sun. This effect increases with the solar zenith angle. This has a very negative side-effect because the spectrometer does not collect all the light transmitted by the collector but only a part coming from a rectangular area that corresponds to the optical image of the slit used in input of the spectrometer to limit the aperture before the grating (the fiber does not blur enough this image to weaken this effect). The combination of the ecentered illumination on the cap in the azimuthal direction of the sun and the collection of the light from another unknown azimuthal direction results in a general azimuthal response of the system. This response is about 5-10% in amplitude, which is unacceptable for measuring albedo with 1% accuracy. To solve this critical problem, we inserted a second flat disc between the fiber and the bumped cap whose



role is to homogenize the light coming from the cap. Moreover, by adding more scattering material, this improves the overall diffusion of the collector and thus the quality of the angular response. We could not have used thicker caps or disks to further improve the scattering because the overall transmissivity of the collector is of the order of 0.001, which imposes relatively long integration time, of the order of 1 second. Longer integration time would result in increasingly uncorrectable dark current and noise. The optimization of the shape of the collector cap was done empirically by a series of trials and errors.

To measure the collector response, we set up an optical bench with a collimated light beam illuminating the collector mounted on a motorized rotation stage. The collector is connected to the spectrometer through a flexible fiber optic. Both the spectrometer and the stage are controlled by computer allowing rapid and reproducible measurements of the irradiance as a function of the incident angle θ . The angular response of the collector $C(\lambda, \theta)$ is calculated as the ratio between the measured irradiance and the ideal cosine response (Section 2.3) so that a value of 1 throughout the spectrum indicates an ideal collector. A typical response is depicted in Figures 4 and 5 as a function of the angle and wavelength respectively. For angles lower than 70° , the deviation remains within $\pm 6\%$ of the ideal response which is comparable to Grenfell et al. (1994) but twice better than Carmagnola et al. (2013) who used a flat collector. The deviation between 70° and 80° degrades significantly which suggests difficulties to get accurate measurements in this range of SZA, however it remains within $\pm 15\%$ while Grenfell et al. (1994) show twice larger errors. The values under 500 nm are extrapolated (Fig. 5) because our light source is too weak in this wavelength range to get signal above noise level. The response is relatively independent of the wavelength for $SZA=50^\circ$ and becomes more and more dependent at larger angles. The measured responses are used for the *ad hoc* correction described in the next section.

2.3 Processing of raw measurements into albedo

The calibration of the raw spectra acquired by the spectrometer requires several processing steps 1) dark and stray light corrections (abbreviated 'dc' and 'sl' hereinafter), 2) integration time scaling ('it'), 3) cross and absolute calibrations ('cal'), 4) cosine correction and cloud detection ('cc'), 5) albedo calculation. These steps are described in details in the following:

Dark and stray light corrections. The raw spectra acquired by the spectrometer are in numerical counts ranging from 0 to about 65000 for each pixel of the CMOS sensor (16-bit Analog-to-Digital converter). As any photo-sensitive sensor, the spectrometer is subject to dark current and other effects that result in non-zero outputs even when no light enters in the device. It is important to remove this offset especially in weak illumination conditions or near the borders of the bandwidth where the sensor sensitivity is weak. The dark current of our spectrometers depends on the temperature and integration times and is most likely subject to aging of the spectrometer and other environmental parameters. Because it is not possible to control all these parameters, dark spectra are measured for every sequence (every 12 min) using the dedicated channel. Acquisitions at two extreme integration times (13 ms the minimum of the spectrometer and 1000 ms the typical time for our measurements) are necessary and sufficient to correct all the spectra acquired during the same sequence at any integration time. We indeed found that the offset is a linear function of the integration time. Hence, to correct a spectrum $S^T(\lambda)$ acquired with a given



integration time T , we first estimate the offset at the actual acquisition time by linear interpolation of the two extreme dark spectra ($D^{T_1}(\lambda)$ and $D^{T_2}(\lambda)$) and then subtract this estimate from the measured spectrum as follows:

$$S_{dc}^T(\lambda) = S^T(\lambda) - \left[\frac{D^{T_2}(\lambda) - D^{T_1}(\lambda, T_1)}{T_2 - T_1} (T - T_1) + D^{T_1}(\lambda, T_1) \right] \quad (1)$$

where $S_{dc}^T(\lambda)$ is the dark current corrected spectrum.

5 Stray light is another typical artifact of spectrometers (Kantzas et al., 2009). It comes from the small fraction of the beam that instead of passing through the grating to be dispersed is deviated and after internal reflexions ends up on the CMOS sensor adding signal to the pixels. Second order dispersion from the grating is another cause of stray light but our spectrometer is mounted with a second-order filter that prevents this effect. For spectrometers of the same brand as ours, Kantzas et al. (2009) found stray light amounting to between 2 and 12% of the maximum intensity. This effect results in an offset which depends
 10 on the total intensity entering the spectrometer. To estimate the stray light, we assume it affects all the pixels equally (i.e. independent of the wavelengths) and estimate it using the average of the counts in the range 200 – 260 nm where no radiation is supposed to come from the grating, because the fiber optics cut-off is around 290 nm and because the weak sensitivity of CMOS sensor in this range. The spectrum corrected from stray light writes:

$$S_{sl+dc}^T(\lambda) = S_{dc}^T(\lambda) - \langle S_{dc}^T(\lambda) \rangle_{\lambda=200-260nm} \quad (2)$$

15 **Integration time scaling.** Considering that the CMOS sensor accumulates charge with the same efficiency whatever the integration time, the spectra in counts are divided by the integration time T to obtain a signal proportional to the incoming radiance:

$$S_{it+sl+dc}(\lambda) = S_{sl+dc}^T(\lambda)/T \quad (3)$$

Calibrations. The calibration of each channel to obtain absolute irradiance is performed in two steps, first the cross-
 20 calibration of the channels to each others and second the absolute calibration of the set. We came to this two-step strategy because it was difficult to design an experiment to perform the absolute calibration directly with a reproducibility better than 1% as required for our target accuracy. Since the albedo only depends on the relative calibration between the channels, we put more effort on the cross-calibration than on the absolute one.

The experiment to obtain data for the cross-calibration consists in measuring successively the upward and downward chan-
 25 nels under the same illumination conditions. To do this, before the installation, we first acquired spectra with the head in normal position, with special care at the horizontal leveling, and performed a second acquisition immediately after flipping the head up side down. The elapsed time between these operations was about 30 s and the experiment was conducted under clear-sky conditions which ensured constant illumination. For each channel, the spectrum taken when looking downward $S_{it+sl+dc}^{cross}(\lambda)$ is used to calibrate any spectra acquired after installation for this particular channel (whatever the direction of looking once
 30 installed) as follows:

$$S_{ccal+it+sl+dc}(\lambda) = \frac{S_{it+sl+dc}(\lambda)}{S_{it+sl+dc}^{cross}(\lambda)} \quad (4)$$



where the *ccal* subscript refers to the cross-calibration step. The downward direction is chosen instead of the upward because the illumination coming from the snow is mostly diffuse which provides a reduced the sensitivity to the head leveling. The experiment was done just before the installation independently for both heads so that it is useful to cross-calibrate both channels of the same head (which is relevant for the albedo) but is inadequate for inter-header calibration.

- 5 The absolute calibration aims at inter-calibrating the heads and provide absolute irradiance (in $\text{W m}^{-2} \text{nm}^{-1}$ for instance). The experiment to collect reference spectra was done after the installation of Autosolexs and uses a commercial spectral radiometer (HR1024, Spectra Vista Corporation) as the reference. Incident spectra have been acquired simultaneously with the two instruments and for the two heads which allows to normalize any spectra acquired later from any channel as follows:

$$S_{cal+it+sl+dc}(\lambda) = S_{ccal+it+sl+dc}(\lambda) \frac{SVC(\lambda)}{S_{ccal+it+sl+dc}^{abs}(\lambda)} \quad (5)$$

- 10 where $SVC(\lambda)$ and $S_{ccal+it+sl+dc}^{abs}$ are the spectra taken with the reference spectral radiometer and Autosolexs respectively. We do not expect an accuracy better than 20% for this step owing to the limited intrinsic accuracy of the reference and the many possible artifacts of the experiment. However this does not affect the albedo uncertainty as explained before.

- Collector angular response correction.** The imperfect angular response of the collector mainly affects the incident channel under clear-sky conditions. Following Grenfell et al. (1994), we use the collector response measured in the laboratory
 15 $C_{it+sl+dc}(\lambda, \theta)$ at different angles θ and corrected for the dark current, stray light and integration time beforehand. The correction is applied to the incident channel only:

$$S_{cal+it+sl+dc}(\lambda) \left[r^{diff}(\lambda, \theta) + (1 - r^{diff}(\lambda, \theta)) \frac{2 \cos \theta}{C_{it+sl+dc}(\lambda, \theta)} \int C_{it+sl+dc}(\lambda, \theta') \sin \theta' d\theta' \right] \quad (6)$$

- where $r^{diff}(\lambda, \theta)$ is the diffuse fraction. The first term in the brackets on the right-hand side represents the diffuse contribution which is assumed isotropic. The anisotropy of the sky diffuse component is neglected which is second order as long as the correction is small. The second term is the direct contribution that is normalized by the collector angular response ($C_{it+sl+dc}(\lambda, \theta)$)
 20 relatively to the ideal cosine ($\cos \theta$).

- The $r^{diff}(\lambda, \theta)$ quantity is estimated using the SBDART atmospheric model (Ricchiuzzi et al., 1998) considering clear-sky conditions. The atmosphere for summer Arctic is used with the altitude adapted to Dome C. The column water vapor totals 0.4 mm (Tremblin et al., 2011) and ozone is set to 300 DU. Aerosol optical depth at 440 nm is set to 0.02. This calculation does
 25 not account for the temporal variations of the atmospheric composition. It could be improved in the future by exploiting the measured incident spectra to infer and better represent the actual atmospheric conditions.

- For the present study, we simply filtered out the data acquired in cloudy conditions. To detect such conditions, the incident spectrum is compared to a spectrum chosen as a reference when the sky was known to be clear (2013-11-15 03:36 UTC close to the local zenith). Each spectrum is then scaled beforehand by the cosine of the solar zenith angle to account for the geometrical
 30 difference. When the scaled spectrum is more than 10% lower than the reference spectrum in the range 405 – 550nm, we consider the sun as being partially obstructed and the data are discarded.



Eventually the spectral albedo is calculated by taking the ratio between the upwelling and downwelling spectra. The shadow of the mat and the heads on the snow surface is very small compared to when an operator takes manual measurements (Carmagnola et al., 2013) and is neglected.

2.4 Specific surface area (SSA) retrieval from spectral albedo

- 5 Snow SSA is obtained by fitting the observed albedo spectra to a theoretical model with SSA as the main unknown. Even if the number of observables per spectrum is very large (up to 2000 different wavelengths), the errors and the auto-correlation between these observations require to keep the number of unknown low to obtain a stable fit. The following assumptions are made: 1) The snowpack is horizontally and vertically homogeneous which means only one SSA value is retrieved. 2) The surface is flat. Roughness which tends to smooth the solar zenith angular response of the snow Warren et al. (1998) is neglected.
- 10 3) The surface and the sensor are horizontal. 4) Snow phase function and single scattering albedo are implicitly described by asymmetry factor, absorption enhancement parameter, and SSA. The values of anisotropy factor and absorption enhancement parameter are taken from Libois et al. (2014b). 5) Snow is clean or contains sufficiently small quantities of impurity not to impact the albedo in the considered wavelength range (Warren et al., 2006).

In these conditions and in the visible and near-infrared wavelengths, the analytical asymptotic radiative transfer (ART, Kokhanovsky and Zege, 2004; Negi et al., 2011) is valid and gives the directional and diffuse hemispheric reflectances α^{diff} and α^{dir} as a function of *SSA*:

$$\alpha^{\text{diff}}(\lambda) = \exp\left(-4\sqrt{\frac{2B\gamma\lambda}{3\rho_{\text{ice}}\text{SSA}(1-g)}}\right) \quad (7)$$

$$\alpha^{\text{dir}}(\lambda, \theta) = \exp\left(-\frac{12}{7}(1+2\cos\theta)\sqrt{\frac{2B\gamma(\lambda)}{3\rho_{\text{ice}}\text{SSA}(1-g)}}\right), \quad (8)$$

where θ is the solar zenith angle, $\rho_{\text{ice}} = 917 \text{ kg m}^{-3}$ is the ice density at 0°C , and $\gamma(\lambda)$ is the absorption coefficient of ice, taken from Warren and Brandt (2008). $B = 1.6$ and $g = 0.85$ are respectively the absorption enhancement and the asymmetry factor values suggested by Libois et al. (2014b).

Considering both direct and diffuse radiations as in Equation (6), the model reads:

$$\alpha^{\text{1-param}}(\lambda, \theta) = [r^{\text{diff}}(\lambda, \theta)\alpha^{\text{diff}}(\lambda) + (1 - r^{\text{diff}}(\lambda, \theta))\alpha^{\text{dir}}(\lambda)], \quad (9)$$

where $r^{\text{diff}}(\lambda, \theta)$ is calculated as for the cosine correction. This model is called hereinafter 1-parameter model because only the SSA is unknown. However, it is not the most suitable because the measurements are often affected by errors which result in a slight wavelength-independent scaling of the albedo. Typical examples include the variations of the illumination between the two successive acquisitions of downwelling and upwelling irradiance, the effect of sloping surface and the imperfection of the cross-calibration. To cope with these errors without negatively impacting the SSA estimation, another model including a free scaling parameter A is also used:

$$30 \quad \alpha^{\text{2-param}}(\lambda, \theta) = A [r^{\text{diff}}(\lambda, \theta)\alpha^{\text{diff}}(\lambda) + (1 - r^{\text{diff}}(\lambda, \theta))\alpha^{\text{dir}}(\lambda)], \quad (10)$$



Nevertheless, considering that a value of A significantly different from 1 reveals a serious issue with the observations, we reject any fit that gives A outside the range 0.9 – 1.1.

The fit is performed with a non-linear least square method (provided by the Python `scipy.optimize.leastsq` function) to minimize the squared difference between the model and observed spectrum. Smoothing is done beforehand to reduce the noise using a first order Butterworth low-pass provided by the Python `scipy.signal.butter` function with cut-off of 0.1.

Given the stronger sensitivity of the albedo to SSA in the near-infrared with respect to the visible, only the data for wavelengths in the range 700 – 1050 nm are used for the fit. This choice is a compromise. Extending the range towards the shorter wavelengths does not bring useful information for the SSA retrieval and may add artifacts, while narrowing it would reduce the number of observations and result in a greater sensitivity to noise. Extending the range in the longer wavelengths is not possible due to the weak sensitivity of the spectrometer.

3 Results

3.1 Stability

Before deriving albedo and SSA over long periods of time, it is important to check the overall stability of the instrument. The seasonal variations of downwelling irradiance are plotted in Figure 6 for the two heads and for the three summer seasons. The irradiance is integrated between 400 and 1000 nm and averaged between 10h – 14h (local time). These data include all weather conditions. Overall, there is a good year to year agreement. For instance, the irradiance observed by the head 1 during the 30 days after the solstice (period in common for the three seasons) has increased by +0.5 % and +4.2% the second and third years with respect to the first one. These values become -0.5%, and +3.0% respectively for the head 2, which is relatively small for an unattended instrument and considering that these values include the inter-annual variability of cloudiness. Only the third season shows a significant increase (around 4-5 %) which is likely due to a degradation of the leveling. The prevailing southerlies winds may have tilted the mast northwards, resulting in the observed increase of the noon irradiances. The influence of tilt angle on the estimation of the SSA is not critical because small geometrical imperfections are partially compensated when using the 2-parameter model that includes the scaling factor A . This influence is evaluated in Section 3.3.2 but we do not know the actual tilt of the heads because the inclinometers mounted on the system appeared to be deficient at low temperature.

3.2 Measurement processing

The different steps to process the raw measurements and obtain albedo are illustrated in this section for two acquisitions taken in two different solar conditions: at local noon the 10 January 2013 with the sun relatively high in the sky for Dome C ($SZA = 53^\circ$) and at 8 pm the same day ($SZA = 77^\circ$). Figure 7 (a) and (b) illustrate the contribution of each step (curves with different colors) for these acquisitions.

The two first steps (dark and stray light corrections) remove the overall offset that is clearly visible in the raw data (Figure 7) at wavelengths where the CMOS sensor has little sensitivity (under 350 nm and around 1100 nm). This correction has a



positive side-effect as it also reduces the small peaks due to damaged pixels like at 862 nm and 1069 nm. With the aging of the spectrometer, the number of such pixels tend to increase (data not shown), but they remain isolated and the correction is efficient.

The albedo is affected by this correction especially near the margins of the spectrum where the sensitivity of the CMOS sensor fades. Because both the incident and reflected spectra are equally affected by the same offset value, the albedo calculated with un-corrected data tends to 1 near the margins. Since clean snow albedo is expected to tend to about 0.98 – 0.99 in the green and blue wavelengths, un-corrected data may appear better, but it is an artifact and the offset really needs to be corrected. At the other side of the spectrum, in the near-infrared, the correction significantly changes the shape of the absorption feature around 1030 nm by lowering the local minimum which has a huge impact on the SSA estimation. Using the procedure described in Section 2.4 on the albedo to estimate SSA, we find that estimated SSA drops from 53 to 41 $\text{m}^2 \text{kg}^{-1}$ after the correction for the noon acquisition and from 61 to 24 $\text{m}^2 \text{kg}^{-1}$ for the evening one. These values highlight the necessity of this correction and consequently the need to accurately measure for each acquisition the dark current and stray light.

The cross and absolute calibration steps (from orange in graph a to violet curve in graph b) also radically change the shape of the spectra. The most visible change on the radiance is mainly due to the absolute calibration because it takes into account the sensitivity of the spectrometer. As expected for a silicon-based sensor, the correction increases the signal in the blue and near-infrared relatively to the yellow and red. Nevertheless, the absolute calibration is not important for the albedo as explained before. The difference on the albedo graphs (c) before (orange curve) and after (violet curve) the calibrations is only due to the cross calibration step between the downward- and upward-looking channels. The correction factor (not shown) linearly decreases from 0.95 in the blue to 0.85 in the near-infrared. Because of this wavelength dependence, the SSA estimation is strongly affected, values decrease from 41 $\text{m}^2 \text{kg}^{-1}$ before correction to 36 $\text{m}^2 \text{kg}^{-1}$ after for the noon acquisition and from 24 $\text{m}^2 \text{kg}^{-1}$ to 20 $\text{m}^2 \text{kg}^{-1}$ for the evening one. This correction is significant but it is worth noting that it is constant over the whole time-series and has therefore no impact on the relative variations of SSA.

In contrast, the collector angular response correction (from violet to pink curves) has very small impact on the radiance (graphs b) whatever the acquisition hour. The impact is also apparently moderate on the albedo graph (c). The correction factor ranges from 0.98 in the blue to 0.99 in the near infra-red at noon and 1.00 to 1.07 at 8 pm. Even if these values are weak (maximum of 7%), the correction removes the decreasing trend in the shorter wavelengths of the visible (400 to 600 nm) that affects the evening acquisition. Albedo measurements by Nicolaus et al. (2010) show a similar artifact. Such a trend is visible throughout the timeseries at large SZA and the collector response correction usually performs well by recovering a nearly constant value as expected.

Regarding SSA estimation, the correction has a little impact for the noon acquisition (36.7 and 36.2 $\text{m}^2 \text{kg}^{-1}$ respectively before and after the correction) as expected. In contrast, for the evening acquisition the SSA estimate increases from 20 $\text{m}^2 \text{kg}^{-1}$ to 35 $\text{m}^2 \text{kg}^{-1}$, the latter being close to the value at noon. This clearly shows that the correction of the collector response is crucial and performs well. The theoretical spectrum that fits the fully-corrected spectrum is shown in black in Figure 7. The differences between the fit and the observation are small, we can note a slight over-estimation at 800 nm and under-estimation at 970 nm which are very likely due to a small error in the refractive index of the ice, since they are not



specific to our instrument (Carmagnola et al., 2013). In contrast, the over-estimation at 1030 nm is more likely an error in the observations resulting from the low sensitivity of the spectrometer in this wavelength range.

To further investigate the impact of the albedo uncertainties due to the instrument artifacts on the retrieved SSA, we use numerical experiments.

5 3.3 Numerical evaluation of the uncertainty

Most artifacts affecting the spectral radiometer results in a first approximation in either an offset in the radiances or a chromatic aberration. To quantify the respective effects of these artifacts on the estimation of the SSA, we perform simple and idealized modeling experiments as follows: we first compute the perfect albedo spectrum with the model described in Equation 7 for a given SSA (called true SSA) and perturb it to mimic the imperfect response of the instrument. Then, we estimate the SSA
 10 using the same procedure as used with real data and deduce the error as the difference between the estimated and true SSA.

3.3.1 Offset

To study the effect of the dark current and stray light correction, we model the measured albedo as:

$$\alpha = \frac{S^{\text{ref}}(\lambda) + d}{S^{\text{inc}}(\lambda) + d}, \quad (11)$$

where the true reflected and incident radiance spectra $S^{\text{ref}}(\lambda)$ and $S^{\text{inc}}(\lambda)$ are affected by an offset d . Dividing by the incident
 15 radiance to make explicit the true albedo α^{true} yields:

$$\alpha(\lambda) = \frac{\alpha^{\text{true}} + \frac{d}{S^{\text{inc}}(\lambda)}}{1 + \frac{d}{S^{\text{inc}}(\lambda)}}. \quad (12)$$

For $S^{\text{inc}}(\lambda)$ we chose a Gaussian shape looking like the raw observations in Figure 7:

$$S^{\text{inc}}(\lambda) = S_{\text{mode}} \exp \left[- \left(\frac{\lambda - 680\text{nm}}{270\text{nm}} \right)^2 \right]. \quad (13)$$

The amplitude of the spectrum S_{mode} is usually of the order of the resolution of the Digital Analog Converter of the spectrometer
 20 (2^{16} in our case) if the integration time is optimal. We define $d' = d/S_{\text{mode}}$, the relative contribution of the offset with respect to the spectrum amplitude. We then estimate the SSA from the perturbed $\alpha(\lambda)$ spectrum and calculate the difference with respect to the true SSA.

To apply this theory to assess the impact of an imprecise dark and stray light correction, we take typical values from the noon acquisition studied in Section 3.2 : the spectrum has an amplitude of nearly 50000 and the offset is around 3800. We
 25 further assume that this offset can be estimated with an accuracy of 10%, which results in a residual bias of 380 and thereby $d' = 0.8\%$. Figure 8 shows the perfect albedo (black curve) calculated for a true SSA of $50 \text{ m}^2 \text{ kg}^{-1}$ and the perturbed albedo (green curve) with $d' = +0.8\%$. Despite the small difference between the spectra, the estimated SSA is $55.4 \text{ m}^2 \text{ kg}^{-1}$ which corresponds to a relatively large over-estimation of 10%, but remains under our criteria of 15%.



To help in designing future spectral radiometer devices, we use the same approach to compute the error in SSA as a function of the relative offset d' ranging from 0 (perfect instrument) to 2% for several SSA values (Figure 9). The result is nearly independent of the true SSA. To meet the 15% criteria, the offset due to dark current and stray light should be corrected with an accuracy better than $d'=1\%$. In theory, such an accuracy can be achieved using a single measurement of one dark pixel as
5 our spectrometer feature a signal-to-noise ratio of 1:500. By averaging many dark pixels, as we do, we ensure an even better accuracy meaning that the offset correction is not an issue in our case. Nevertheless, it is worth noting that we assume the stray light effect to be uniform on all the pixels of the CMOS sensor. If this is not the case, the correction of the stray light would require a more complex method and the evaluation of the error proposed here would be only a lower bound of the error.

3.3.2 Chromatic aberration

10 To investigate the effect of chromatic aberration, we consider the true albedo is multiplied by a linear function of the wavelength:

$$\alpha = \left(1 - b \frac{\lambda - \lambda_0}{\lambda_1 - \lambda_0}\right) \alpha^{\text{dir}}(\lambda, \theta) \quad (14)$$

where b controls the slope of the wavelength dependence. The limits $\lambda_0=400$ nm and $\lambda_1=1100$ nm are chosen so that the instrument is assumed perfect at 400 nm in the blue and b represents the differential response of the upward and downward
15 looking channels at 1100 nm. Figure 10 illustrates the results with true SSA of $50 \text{ m}^2 \text{ kg}^{-1}$ and $b = 0.05$ (see below for actual values of b). We remind that the SSA estimation only uses data between 700 – 1050 nm. The SSA is estimated to $38.2 \text{ m}^2 \text{ kg}^{-1}$ by the 2-parameter model and $27.6 \text{ m}^2 \text{ kg}^{-1}$ for 1-parameter one. This corresponds to relative error of 24% and 45% respectively. The 2-parameter model is clearly better which can be explained by the fact that it is insensitive to the scaling of the albedo but relies mostly on the relative variations of albedo over the wavelength range used for the optimization. However,
20 this error is larger than the 15% target accuracy.

An interesting feature of the 2-parameter model is that the albedo predicted with the optimal SSA and A values (orange curve) exhibits a bias in the visible not only with respect to the true albedo (black curve) but also to the observed one (green curve). For instance, in Figure 10, the difference is 0.024 on average over the range 400 – 550 nm. This difference (residuals hereinafter) is a consequence of the wavelength-dependent perturbation and can be exploited to assess the amplitude of this
25 perturbation in real data because it does not require knowledge of the true SSA. It means that the acquisitions subject to residual chromatic aberration should feature a large difference in the visible range with respect to the spectrum predicted using the 2-parameter model. The previous calculation with $b = 0.05$ and true SSA= $50 \text{ m}^2 \text{ kg}^{-1}$ gives a difference of 0.024 and was found to corresponds to relative error of 24% of SSA. To explore how these values vary in other conditions, we perform several simulations. Figure 11a shows the relative error and the mean difference over the range 400 – 550 nm as a function of the
30 chromaticity parameter b for several SSA. The error varies almost linearly with b and the slope increases with SSA. Hence, to attain the target accuracy of 15%, the chromatic parameter should not exceed about 0.04 for SSA= $20 \text{ m}^2 \text{ kg}^{-1}$ and even less, 0.02, for SSA= $100 \text{ m}^2 \text{ kg}^{-1}$. Figure 11b shows the univocal relationship between b and the mean residual. This result suggests that mean residual values under 0.01 indicate a chromaticity better than 0.02 and thus an SSA accuracy better than 15%.



We apply this criteria on the real data by calculating the albedo spectrum predicted by 2-parameter model using the optimal SSA and A obtained by fitting the model to the observations in the range 700 – 1050 nm. We then calculate the mean difference in the range 400 – 550 nm and reject the acquisition if this difference is larger than 0.01. The skills of this filter are illustrated in the next section. It is worth noting that it can only work if the light-absorbing impurities are negligible because dust or black carbon usually lead to a decrease of the albedo in the blue-green (Warren, 1982) which would be interpreted as an artifact by our filter that is based on pure snow albedo calculation.

It is interesting to estimate the chromatic aberration associated with the different steps of the processing or other external sources of error. For instance, the cross-calibration factor ranges from 0.95 in the blue to 0.85 in the infrared (Section 3.2) which corresponds to approximately $b = 0.10$. It means that the cross-calibration is definitely required to reach the 15% accuracy. If we assume that the correction factor is accurate within 10%, for instance because of the limited reproducibility of the experiment to determine the reference spectra, it leads to a residual trend of $b \approx 0.01$ which is weak enough to reach the 15% accuracy. A similar conclusion can be drawn for the collector angular response correction that resulted in similar scaling factors, between 1.00 to 1.07 for the blue and near infra-red wavelengths respectively for the evening acquisition studied in Section 3.2 and much lower factors for the noon acquisition.

Errors of the leveling of the measurement heads also indirectly results in chromatic aberration because it affects the direct/diffuse balance. Following Bogren et al. (2015) and Grenfell et al. (1994), the albedo error $\eta(\lambda, \theta)$ due to a tilt angle δ in the direction of the sun (worse case) can be written:

$$\eta(\lambda, \theta) \approx (1 - r^{\text{diff}}(\lambda, \theta)) \left(\frac{\cos(\theta - \delta)}{\cos(\theta)} - 1 \right) \quad (15)$$

$$(16)$$

where the diffuse term error has been neglected as suggested by Bogren et al. (2015) results. Considering small errors, b can be estimated as follows:

$$b \approx \eta(\lambda_1, \theta) - \eta(\lambda_0, \theta) \quad (17)$$

$$\approx (r^{\text{diff}}(\lambda_1, \theta) - r^{\text{diff}}(\lambda_0, \theta)) \left(\frac{\cos(\theta - \delta)}{\cos(\theta)} - 1 \right) \quad (18)$$

For a tilt angle of 1° and under Dome C typical conditions, we obtain $b = 0.01$ for $SZA=53^\circ$ (as the noon acquisition studied in Section 3.2) and $b = 0.05$ for $SZA=77^\circ$ (as the evening acquisition) which is weak in the former case but is too high in the latter one to reach the 15% target accuracy. These results highlight the crucial role of the leveling of the instrument. When, Autosolex was installed, the leveling was carefully done within the uncertainty allowed by spirit level (about 0.2°) but it is likely that it has degraded over time. Given that measuring tilt angle with electronic devices in Dome C winter conditions is challenging and that the instrument was not serviced to preserve the surface, the confidence in our data is based on the *ad hoc* filtering based on the 2-parameter model residual in the visible.

The effect of the different artifacts has been evaluated independently of each other, but in real data, they combine, sometimes compensating, sometimes not. The assessment of the interactions between the artifacts is difficult and is not addressed here, but reaching 15% accuracy in real data may require stricter tuning of the filters.



3.4 Diurnal cycle of SSA

The SSA estimated over the course of a day is depicted in Figure 12a for the two heads for the 10 January 2013 as a function of the local hour and the corresponding SZA. Gray symbols represent data rejected for one of the three reasons: presence of clouds, chromatic aberration or A outside the range 0.9 – 1.1.

5 This particular day clouds were detected only at 3:25 and after 21:00 but the detection may not be reliable at high SZA because of the simplistic approach used to scale the reference spectrum to a given SZA (Section 2.3). The other cases of rejection are equally due to the two other criteria. It appears clearly that it usually happens when the sun is low on the horizon, with a SZA higher than 70° , which is expected. However, in many cases, the SSA of rejected acquisitions is close to valid ones which could indicate that our criteria are too conservative. On the other hand, some data at very high SZA are not rejected
10 while we believe they should have been. For this reason, we let the criteria being conservative and even discarded acquisitions at SZA higher than 75° in the following.

Valid data show small diurnal variations between 32 and 35 $\text{m}^2 \text{kg}^{-1}$ for head 1 and slightly larger between 31 and 40 $\text{m}^2 \text{kg}^{-1}$ for head 2. Root mean squared variations is respectively 0.9 and 2.6 $\text{m}^2 \text{kg}^{-1}$ which is well under the 15% target accuracy. The mean difference between both heads is 2.6 $\text{m}^2 \text{kg}^{-1}$. The nearly perfect symmetry around noon suggests that
15 these variations are not do not come from real SSA variations but are rather errors linked to SZA either due to uncorrected artifacts in the observations or limitation of the theoretical model used for the estimation.

The diurnal cycle for one day later in the summer season is shown in Figure 12b (1 March 2013). The SSA is much higher than in the previous case and the number of hours with SZA lower than 75° is more limited. In addition, more data are rejected, mostly because of the chromatic aberration. All together, the valid values range between 53 and 74 $\text{m}^2 \text{kg}^{-1}$ representing a
20 large amplitude of 30%. The standard deviation is about 3.5 $\text{m}^2 \text{kg}^{-1}$ for both heads, that is 10% for a $\pm 1\sigma$ variation. It was impossible to determine whether these variations are real or result from measurement and retrieval errors. These variations must therefore be interpreted as an upper bound estimate of the uncertainty of the retrieved SSA.

3.5 Statistical characteristic of the seasonal variations

The seasonal variations of SSA estimated from the two heads over three summers (December 2012 to March 2015) are shown
25 in Figure 13. The daily mean of valid data is plotted in color and each individual valid data is shown in gray in the background to give an idea of the diurnal variability (or maybe residual error). In this paper, we perform a quality assessment of this series leaving the interpretation of the geophysical features to (Libois et al., 2015).

At the beginning and end of the seasons, the SSA is usually high and exhibits large day to day variations that are suspicious. Several issues like the those due to high SZA, the weaker sensitivity of the SSA – albedo relationship at higher SSA (Domine
30 et al., 2006; Gallet et al., 2009) and the lower number of valid data entering the daily mean during these periods with short daylight, probably combine during these periods. Because of this lower quality, the time-series in Libois et al. (2015) only uses noon data to minimize the high SZA issue and is limited to SZA lower than 67° which corresponds at Dome C to the period 18 October to 27 February. Here, because we introduce the filter based on the detection of chromatic aberration, we apply the



algorithm for SZA up to 75° , relying on the filter to reject low quality data at high SZA. As a result, the period presented is slightly longer (about two weeks each sides but with little data), but the interpretation at the extremes is still subject to caution. Using the daily mean of the valid data instead of the noon value has very little impact, the difference ranges between -1.0 and $+1.5 \text{ m}^2 \text{ kg}^{-1}$ depending on the season and head.

5 The two heads give very close values (within the daily range of variation) for some periods while significant differences are observed for others usually in the spring (October 2013 and most remarkably October-November 2104) and in the fall (March 2013 and 2014). If we consider December-January to assess the statistics, we find the difference between heads 1 and 2 to be -2.7 , 1.0 and $0.0 \text{ m}^2 \text{ kg}^{-1}$ on average and 3.2 , 2.4 and $2.2 \text{ m}^2 \text{ kg}^{-1}$ root mean square (rms), respectively for the three seasons. This rules out any significant bias between the two heads which could have come from issues with the cross-calibration,
10 the only processing step that uses different data depending to the head. This also indicates that the seasonal stability of the instrument and processing is of the same order as the diurnal standard deviation (Section 3.4). Conversely, it means that the difference observed during some periods is due to difference of SSA between the footprints of the two heads (Section 3.6).

All together these results converge to a precision much better than the targeted 15% which allows to safely interpret the seasonal variations as a geophysical signal (Libois et al., 2015). However, it does not presume of the absolute accuracy which
15 mostly depends on the validity of the model in general and the choice of the parameter values (shape factors, assumption of a flat surface...) in particular.

3.6 Representativeness of the estimated SSA: horizontal variability

Both heads depict an overall seasonal decrease from values higher than $60 - 80 \text{ m}^2 \text{ kg}^{-1}$ in October to a minimum around $25 \text{ m}^2 \text{ kg}^{-1}$ occurring in January and/or February. While they show very similar values during some periods, significant
20 differences occur during others. The two heads are located 2-m apart. Being at 2 m above the surface and accounting for the cosine weighting of the collector, we can estimate that 50% of the signal they receive from the surface is reflected from a disk of 2 m in radius (12 m^2 in surface area), and 75% from 3.5 m in radius (38 m^2). Despite the proximity and a slight partial overlap of the footprints, differences between the two heads can be particularly marked as in Spring 2014. We could invoke the fact that snow accumulation is known to be an irregular and heterogeneous process at Dome C (Petit et al., 1982; Libois et al.,
25 2014a). However, this argument is not compatible with the lack of difference observed in the summers between the two heads while several precipitation events do occur (Libois et al., 2015) and have a clear impact on SSA.

In spring 2014, the large and persistent difference could be ascribed to the presence of an erosional feature under head 1 (Figure 1) and a wind-form feature (elongated dune) under head 2. The latter could be composed of recently deposited snow while the former feature sastrugi and older snow layers emerging on the surface. Nevertheless, this interpretation is subject to
30 caution because visible photography is insensitive to SSA, as evidenced by the weak difference between the two pictures taken 12 October and 27 November despite a three-fold decrease of the SSA.

The diurnal cycles of the estimated SSA during spring 2014 is small compared to the difference between the heads, which suggests the difference between the two heads is significant, but the cycle is not symmetrical with respect to noon (not shown) as opposed to the cycles shown in Figure 12. This could be caused by the inhomogeneity of the surface SSA. Since the surface



is particularly rough and the sun low on the horizon during this period, the shadows are significant and change with the solar time. Hence, the "average" spectrum measured by the instrument comes from different areas depending on the time of the day and those areas may have different SSA. The direct effect of the roughness could also affect the symmetry of the diurnal cycle when the surface is rough but assessing the spectral effect of the roughness is difficult and beyond the scope of this study.

5 3.7 Representativeness of the estimated SSA: vertical gradient

A straightforward approach to determine the validity and accuracy of the instruments and algorithm is to compare estimated SSA with manual measurements optical devices like ASSSAP (Arnaud et al., 2011; Libois et al., 2015). Although this device uses similar principles to the algorithm presented in Section 2.4, an important difference is the use of a longer wavelength (1310 nm) resulting in a significant difference in the depths probed by both instruments.

10 Figure 14 shows individual manual measurements taken during the 2013-2014 seasons with ASSSAP along with Autosolexs SSA time-series (average of the two heads). Measurements of surface snow SSA with ASSSAP follow a specific protocol that takes care to preserve the surface and prevent post-sampling transformation of the snow. More than 5 manual measurements were taken every day in a site located approximately 1 km from Autosolexs. The sampling strategy was not random but aimed at covering the variety of different surface facies identified by the operator. It implies that the average of the values may differ
15 from the true areal average of SSA when the spread of SSA is large. Figure 14 clearly shows that most manual measurements significantly differ from the SSA estimated from Autosolexs. However the lowest values seem to agree with Autosolexs during the first part of the season, until about 8 January. After this, the spread of manual measurements is significantly reduced and despite higher values of SSA with ASSSAP, the temporal variations are correlated with those of Autosolexs.

Although this comparison does not help validate or estimate the accuracy of Autosolexs SSA, it clearly demonstrates that
20 both SSA – abusively qualified of surface snow SSA – are representative of different thicknesses owing to the different wavelengths used by the respective instruments which combines with a sharp gradient of SSA in the first millimeters under the surface.

The first study to suggest such a gradient is Grenfell et al. (1994). They found at South Pole that adding a thin layer of very small snow grains (over $100 \text{ m}^2 \text{ kg}^{-1}$) on the surface in their radiative transfer calculations was required to match their
25 albedo measurements. Carmagnola et al. (2013) at Summit Greenland uses spectral data in the wavelength range encompassing Autosolexs and ASSSAP operating ranges and found that tuning the surface layer SSA helps to improve the agreement with the observations but did not explore values as high as Grenfell et al. (1994) did. In contrast, Gallet et al. (2011) measured SSA vertical profiles at Dome C and obtained radiative transfer calculations in agreement with Hudson et al. (2006) observations without adding such a layer. Using snowpack numerical modeling, Libois et al. (2015) obtained SSA profiles at Dome C with
30 a sharp gradient near the surface. It is worth noting that their simulation uses ERA-Interim as input which forecasts occasional precipitation events leading to marked rises of SSA (Figure 13 but does not forecast clear-sky precipitation (a.k.a diamond dust) despite its frequent observation at Dome C. This indicates that diamond dust is not required in the model to get a sustained high surface SSA and that including the diamond dust in the simulation could increase even more the predicted gradient. We



can conclude that a sharp SSA gradient in the first uppermost centimeters exists with SSA possibly exceeding $100 \text{ m}^2 \text{ kg}^{-1}$ on the very surface and that this gradient persists over long periods, even during periods without precipitation.

As a consequence, the vertical representativeness of the SSA estimated in this study is an important information in order to analyze the data and compare them to models or other observations. It is therefore important to determine the thickness of the layer sampled by Autosolexs. The answer is not straightforward nor univocal because the penetration depth of radiation depends on the wavelength and the vertical profile of snow properties, including SSA itself and density. Furthermore, the estimated SSA value is not a simple average over a given thickness but is weighted by a decreasing function of the depth. This function is exponential if the snow is homogeneous, but more complex otherwise.

Only radiative transfer calculations can give a precise estimation of the weight function. To evaluate it for an homogeneous snowpack, we run the two-stream radiative transfer model TARTES (Libois et al., 2013) considering a semi-infinite medium with a density of 270 kg m^{-3} corresponding to mean surface conditions (Libois et al., 2014a) and a fixed SSA. A layer with variable thickness h is added on top of it, with the same properties, excepted that a small perturbation is added to the SSA (e.g. $+1 \text{ m}^2 \text{ kg}^{-1}$, but the exact value does not alter the final result as long as it is small compared to the actual value of SSA). The relative contribution of the uppermost layer to the albedo is then defined as the quantity $(\alpha(h) - \alpha(0))/(\alpha(\infty) - \alpha(0))$ where $\alpha(h)$ is the albedo calculated by TARTES for the thickness h and averaged over the wavelength range used by Autosolexs (700-1050 nm). The contribution is shown in Figure 15 (plain line) as a function of h for different SSA values. Results show that the uppermost 10 mm snow layer contributes to nearly 60% of the albedo for SSA of $20 \text{ m}^2 \text{ kg}^{-1}$ and 85% for higher SSA of $100 \text{ m}^2 \text{ kg}^{-1}$. Conversely, the layer contributing to 80% of the signal is 18, 12 and 8mm thick for SSA of 20, 50 and 100 respectively. As a conclusion, 1 cm is a good approximation for typical Dome C conditions. Similar simulations have been run at 1310 nm to illustrate the difference with ASSSAP (dash line in Figure 15). In this case most of the signal comes from uppermost 5 mm, at most, in any conditions. Note that this depth is inversely proportional to the density so that the thickness values presented here should be multiplied by about two in case of fresh snow or surface hoar.

The question of the representativeness of the SSA estimated with the instruments is relevant for comparing the observations with snow models like Crocus or to study the snow processes. As far as the broadband albedo and the surface radiative budget are concerned, SSA estimated in the range 700 – 1050 nm is the most relevant as most of the solar energy is absorbed in the near-infrared range (Gardner and Sharp, 2010).

4 Discussions and Conclusion

This study presents Autosolexs, a multi-channel spectral radiometer used to automatically measure spectral albedo in the visible and near infrared range (under 1000 nm) and an algorithm to retrieve the surface specific area of the surface snow. Despite the specificity of this home-made instrument and the operating conditions of Dome C, several general recommendations can be made regarding the design and deployment of such devices: 1) Using fiber optics to transmit the light make possible to bury the temperature-sensitive components of the instrument under the snow. This was necessary for Dome C considering that temperature is frequently below -40°C even during the daylight. Maintaining the device at constant above freezing temperature



avoids deterioration and drift of the spectrometer. However, it costs some energy which would require adequate dimensioning of solar panels or wind turbines in the case of autonomous stations. The instrument has been working since December 2012, even in winter, with only a few short interruptions due to power outage. 2) Use of optical switch instead of two or more spectrometers is a good option. It is cost effective, avoids the need of inter-calibration of the spectrometers (Nicolaus et al., 2010) which may drift independently over time (France et al., 2011) but it is subject to switching delay and reproducibility, and involves mechanical parts. It allowed us to deploy 2 measurement heads located a few meters apart which provided evidence of spatial difference during some periods. With a 16-channel optical switch, it is technically possible to set up 7 measurement heads 3) The leveling of the head should be and remain horizontal not only for albedo which has been highlighted by numerous authors (e.g. Bogren et al., 2015), but also for SSA retrieval. Under typical polar summer conditions or in winter in the mid-latitudes, we estimate the leveling must be better than 1° to get at least the noon acquisition accurate enough to retrieve estimate SSA with an accuracy of 15%. Maintaining automatically the leveling or measuring the inclination at low temperature is challenging. 4) Designing good collectors and correcting from their imperfect response is necessary for SZA above 60° and becomes more and more difficult above 70° . The determination of the atmospheric diffuse/direct ratio and cloud mask deserves further work compared to what has been achieved here. Using the measured incident spectrum to infer the actual ratio is an avenue. 5) Filtering data based on the difference between observed and estimated albedo in the visible range allows to discard data subject to any artifact that produces chromatic aberration. The approach developed here does not require high spectral resolution data, it can be applied to multi-band radiometers like those carried by satellites. However, it requires some assumptions like negligible impurity content and could interfere with the atmospheric correction often based on the blue channels for space-borne sensors.

Part of the difficulties addressed in this study arises from the weak sensitivity of the SSA-reflectance relationship at wavelengths under $1 \mu\text{m}$, especially for the high SSA encountered at Dome C ($50 \text{ m}^2 \text{ kg}^{-1}$ and higher) (Domine et al., 2006; Gallet et al., 2009). Extending the present instrument further in the infrared seems attractive because the sensitivity to SSA is greater so that larger error on the albedo measurement would be acceptable for a similar target accuracy of SSA. However it comes at a price. Building light collectors with a good angular response is increasingly challenging at longer wavelengths due to the decreasing scattering. The balance between theoretically more sensitive wavelengths and increasing chromatic aberrations needs to be weighted.

The influence of the surface roughness on the albedo and estimated SSA also deserves further work. Warren et al. (1998) explained that "introducing roughness will cause no change to the albedo of a surface whose albedo is 0.0 or 1.0. The greatest effect is for intermediate values of albedo; in the case of snow, this means near-infrared wavelength" which implies that roughness change tends to reduce the albedo in the 1030 nm absorption feature more than at shorter wavelengths where it is closer to 1. This implies that our algorithm, by assuming a flat interface, would under-estimate the SSA over rough surfaces. Moreover, with measurements heads only 2 m above the surface, the scale of the measurements and that of the roughnesses are of the same order resulting in a more complex problem than that considered in modeling studies (Leroux and Fily, 1998). Spatial survey of albedo and SSA variations could be used to evaluate this effect. The anisotropy of the roughness and the slope of the terrain (relevant to mountainous regions only) are expected to introduce a spurious diurnal cycle and need to be considered in the future as well.



The present study, by retrieving 3-year long time series of SSA, confirms the general coarsening of snow grains during the summer observed in several studies (Jin et al., 2008; Picard et al., 2012) and recently shown to be predicably by snow metamorphism modeling (Libois et al., 2015). However, despite its length, it features relatively little inter-annual variations compared to that observed by satellite and provides little evidence yet of modulation of the grain size by precipitation at the seasonal timescale as hypothesized by Picard et al. (2012). An important perspective of this work is to maintain Autosolexs at Dome C and to develop the installation of ground-based spectral radiometers in Antarctica.

Data Availability

The corrected and quality-checked albedo spectra and SSA time-series will be available from the Pangea database once the peer-reviewed process has validated the method.

10 *Author contributions.* G. Picard and L. Arnaud developed and built Autosolexs, L. Arnaud and Q. Libois deployed it at Dome C and performed the calibration experiments. G. Verin performed the collector characterization. M. Dumont conducted the atmospheric simulations. G. Picard and Q. Libois developed the retrieval algorithm and prepared the manuscript with contributions from the other authors.

15 *Acknowledgements.* This study was supported by the ANR program 1-JS56-005-01 MONISNOW. The authors acknowledge the French Polar Institute (IPEV) for the financial and logistic support at Concordia station in Antarctica through the NIVO program. This work has also been supported by a grant from OSUG@2020 (investissement d'avenir – ANR10 LABX56). We thank the winter-over staff at Concordia for the maintenance of Autosolexs.



References

- Aoki, T., Aoki, T., Fukabori, M., Hachikubo, A., Tachibana, Y., and Nishio, F.: Effects of snow physical parameters on spectral albedo and bidirectional reflectance of snow surface, *J. Geophys. Res.*, 105, 10 219–10 236, doi:10.1029/1999JD901122, 2000.
- Arnaud, L., Picard, G., Champollion, N., Domine, F., Gallet, J., Lefebvre, E., Fily, M., and Barnola, J.: Measurement of vertical profiles of snow specific surface area with a 1 cm resolution using infrared reflectance: instrument description and validation, *J. Glaciol.*, 57, 17–29, doi:10.3189/002214311795306664, 2011.
- Bernhard, G. and Seckmeyer, G.: New Entrance Optics for Solar Spectral UV Measurements, *Photochem Photobiol.*, 65, 923–930, doi:10.1111/j.1751-1097.1997.tb07949.x, <http://dx.doi.org/10.1111/j.1751-1097.1997.tb07949.x>, 1997.
- Bogren, W. S., Burkhart, J. F., and Kylling, A.: Tilt error in cryospheric surface radiation measurements at high latitudes: a model study, *The Cryosphere Discussions*, 9, 4355–4376, doi:10.5194/tcd-9-4355-2015, <http://dx.doi.org/10.5194/tcd-9-4355-2015>, 2015.
- Carmagnola, C. M., Domine, F., Dumont, M., Wright, P., Strellis, B., Bergin, M., Dibb, J., Picard, G., Libois, Q., Arnaud, L., and et al.: Snow spectral albedo at Summit, Greenland: measurements and numerical simulations based on physical and chemical properties of the snowpack, *The Cryosphere*, 7, 1139–1160, doi:10.5194/tc-7-1139-2013, <http://dx.doi.org/10.5194/tc-7-1139-2013>, 2013.
- Curry, J. A., Schramm, J. L., and Ebert, E. E.: Sea Ice-Albedo Climate Feedback Mechanism, *J. Climate*, 8, 240–247, doi:10.1175/1520-0442(1995)008<0240:siacfm>2.0.co;2, [http://dx.doi.org/10.1175/1520-0442\(1995\)008<0240:SIACFM>2.0.CO;2](http://dx.doi.org/10.1175/1520-0442(1995)008<0240:SIACFM>2.0.CO;2), 1995.
- Domine, F., Salvatori, R., Legagneux, L., Salzano, R., Fily, M., and Casacchia, R.: Correlation between the specific surface area and the short wave infrared (SWIR) reflectance of snow, *Cold Reg. Sci. Technol.*, 46, 60–68, doi:10.1016/j.coldregions.2006.06.002, 2006.
- Dumont, M., Brissaud, O., Picard, G., Schmitt, B., Gallet, J., and Arnaud, Y.: High-accuracy measurements of snow Bidirectional Reflectance Distribution Function at visible and NIR wavelengths - comparison with modelling results, *Atmos. Chem. Phys.*, 10, 2507–2520, doi:10.5194/acp-10-2507-2010, <http://www.atmos-chem-phys.net/10/2507/2010/>, 2010.
- Ettema, J., van den Broeke, M. R., van Meijgaard, E., and van de Berg, W. J.: Climate of the Greenland ice sheet using a high-resolution climate model – Part 2: Near-surface climate and energy balance, *The Cryosphere*, 4, 529–544, doi:10.5194/tc-4-529-2010, <http://dx.doi.org/10.5194/tc-4-529-2010>, 2010.
- Fierz, C., Armstrong, R. L., Durand, Y., Etchevers, P., Greene, E., McClung, D. M., Nishimura, K., Satyawali, P. K., and Sokratov, S. A.: The international classification for seasonal snow on the ground, UNESCO/IHP, 2009.
- France, J. L., King, M. D., Frey, M. M., Erbland, J., Picard, G., MacArthur, A., and Savarino, J.: Snow optical properties at Dome C, Antarctica - implications for snow emissions and snow chemistry of reactive nitrogen, *Atmospheric Chemistry and Physics Discussions*, 11, 11 959–11 993, doi:10.5194/acpd-11-11959-2011, <http://www.atmos-chem-phys-discuss.net/11/11959/2011/>, 2011.
- Gallet, J., Domine, F., Arnaud, L., Picard, G., and Savarino, J.: Vertical profile of the specific surface area and density of the snow at Dome C and on a transect to Dumont D’Urville, Antarctica – albedo calculations and comparison to remote sensing products, *The Cryosphere*, 5, 631–649, doi:10.5194/tc-5-631-2011, <http://www.the-cryosphere.net/5/631/2011/>, 2011.
- Gallet, J. C., Domine, F., Zender, C. S., and Picard, G.: Measurement of the specific surface area of snow using infrared reflectance in an integrating sphere at 1310 and 1550 nm, *The Cryosphere*, 3, 167–182, 2009.
- Gardner, A. S. and Sharp, M. J.: A review of snow and ice albedo and the development of a new physically based broadband albedo parameterization, *Journal of Geophysical Research*, 115, doi:10.1029/2009jf001444, <http://dx.doi.org/10.1029/2009JF001444>, 2010.
- Goelles, T., Bøggild, C., and Greve, R.: Ice sheet mass loss caused by dust and black carbon accumulation, *The Cryosphere Discussions*, 9, 2563–2596, 2015.



- Grenfell, T. C. and Warren, S. G.: Representation of a nonspherical ice particle by a collection of independent spheres for scattering and absorption of radiation, *J. Geophys. Res.*, 104, 31 697–31 710, doi:10.1029/1999JD900496, 1999.
- Grenfell, T. C., Warren, S. G., and Mullen, P. C.: Reflection of solar radiation by the Antarctic snow surface at ultraviolet, visible, and near-infrared wavelengths, *Journal of Geophysical Research*, 99, 18 669–18 684, doi:10.1029/94JD01484, <http://www.agu.org/pubs/crossref/1994/94JD01484.shtml>, 1994.
- Hudson, S. R. and Warren, S. G.: An explanation for the effect of clouds over snow on the top-of-atmosphere bidirectional reflectance, *Journal of Geophysical Research*, 112, doi:10.1029/2007JD008541, <http://www.agu.org/pubs/crossref/2007/2007JD008541.shtml>, 2007.
- Hudson, S. R., Warren, S. G., Brandt, R. E., Grenfell, T. C., and Six, D.: Spectral bidirectional reflectance of Antarctic snow: Measurements and parameterization, *Journal of Geophysical Research*, 111, doi:10.1029/2006jd007290, <http://dx.doi.org/10.1029/2006JD007290>, 2006.
- 5 Jin, Z., Charlock, T. P., Yang, P., Xie, Y., and Miller, W.: Snow optical properties for different particle shapes with application to snow grain size retrieval and MODIS/CERES radiance comparison over Antarctica, *Remote Sens. Environ.*, 112, 3563–3581, 2008.
- Kantzas, E. P., McGonigle, A. J. S., and Bryant, R. G.: Comparison of Low Cost Miniature Spectrometers for Volcanic SO₂ Emission Measurements, *Sensors*, 9, 3256–3268, doi:10.3390/s90503256, <http://dx.doi.org/10.3390/s90503256>, 2009.
- Kokhanovsky, A. A. and Zege, E. P.: Scattering optics of snow, *Appl. Optics*, 43, 1589–1602, 2004.
- 15 Kuchiki, K., Aoki, T., Niwano, M., Motoyoshi, H., and Iwabuchi, H.: Effect of sastrugi on snow bidirectional reflectance and its application to MODIS data, *Journal of Geophysical Research*, 116, doi:10.1029/2011jd016070, <http://dx.doi.org/10.1029/2011JD016070>, 2011.
- Leroux, C. and Fily, M.: Modeling the effect of sastrugi on snow reflectance, *Journal of Geophysical Research*, 103, 25 779, doi:10.1029/98je00558, <http://dx.doi.org/10.1029/98JE00558>, 1998.
- Libois, Q., Picard, G., France, J. L., Arnaud, L., Dumont, M., Carmagnola, C., and King, M. D.: Grain shape influence on light extinction in snow, *The Cryosphere*, to be submitted, 2013.
- 20 Libois, Q., Picard, G., Arnaud, L., Morin, S., and Brun, E.: Modeling the impact of snow drift on the decameter-scale variability of snow properties on the Antarctic Plateau, *J. Geophys. Res. Atmos.*, 119, 11,662–11,681, doi:10.1002/2014jd022361, <http://dx.doi.org/10.1002/2014JD022361>, 2014a.
- Libois, Q., Picard, G., Dumont, M., Arnaud, L., Sergent, C., Pougatch, E., Sudul, M., and D., V.: Experimental determination of the absorption enhancement parameter of snow, *J. of Glaciology*, 60, 714–724, doi:10.3189/2014jog14j015, <http://dx.doi.org/10.3189/2014JoG14J015>, 2014b.
- 25 Libois, Q., Picard, G., Arnaud, L., Dumont, M., Lafaysse, M., Morin, S., and Lefebvre, E.: Summertime evolution of snow specific surface area close to the surface on the Antarctic Plateau, *The Cryosphere Discussions*, 9, 4499–4538, doi:10.5194/tcd-9-4499-2015, <http://dx.doi.org/10.5194/tcd-9-4499-2015>, 2015.
- 30 Macke, A. and Mishchenko, M. I.: Applicability of regular particle shapes in light scattering calculations for atmospheric ice particles, *Appl. Optics*, 35, 4291, doi:10.1364/AO.35.004291, <http://www.opticsinfobase.org/abstract.cfm?URI=ao-35-21-4291>, 1996.
- Marks, A., Fragiaco, C., MacArthur, A., Zibordi, G., Fox, N., and King, M. D.: Characterisation of the HDRF (as a proxy for BRDF) of snow surfaces at Dome C, Antarctica, for the inter-calibration and inter-comparison of satellite optical data, *Remote Sensing of Environment*, 158, 407–416, doi:10.1016/j.rse.2014.11.013, <http://dx.doi.org/10.1016/j.rse.2014.11.013>, 2015.
- 35 Mary, A., Dumont, M., Dedieu, J.-P., Durand, Y., Sirguey, P., Milhem, H., Mestre, O., Negi, H. S., Kokhanovsky, A. A., Lafaysse, M., and et al.: Intercomparison of retrieval algorithms for the specific surface area of snow from near-infrared satellite data in mountainous terrain, and comparison with the output of a semi-distributed snowpack model, *The Cryosphere*, 7, 741–761, doi:10.5194/tc-7-741-2013, <http://dx.doi.org/10.5194/tc-7-741-2013>, 2013.



- Matzl, M. and Schneebeli, M.: Measuring specific surface area of snow by near-infrared photography, *J. Glaciol.*, 52, 558–564(7), doi:10.3189/172756506781828412, 2006.
- Morin, S., Domine, F., Dufour, A., Lejeune, Y., Lesaffre, B., Willemet, J.-M., Carmagnola, C., and Jacobi, H.-W.: Measurements and modeling of the vertical profile of specific surface area of an alpine snowpack, *Advances in Water Resources*, 55, 111–120, doi:10.1016/j.advwatres.2012.01.010, <http://dx.doi.org/10.1016/j.advwatres.2012.01.010>, 2013.
- Morrow, J., Goebel, D., Booth, C., and Reynolds, R.: The impact of cosine collector geometry on aquatic spectroradiometer performance, *OCEANS 2000 MTS/IEEE Conference and Exhibition. Conference Proceedings (Cat. No.00CH37158)*, doi:10.1109/oceans.2000.882233, <http://dx.doi.org/10.1109/OCEANS.2000.882233>, 2000.
- Myhre, G., Shindell, D., Bréon, F.-M., Collins, W., Fuglestedt, J., Huang, J., Koch, D., Lamarque, J.-F., Lee, D., Mendoza, B., Nakajima, T., Robock, A., Stephens, G., Takemura, T., and Zhang, H.: Anthropogenic and Natural Radiative Forcing, *Climate Change 2013 - The Physical Science Basis*, p. 659–740, doi:10.1017/cbo9781107415324.018, <http://dx.doi.org/10.1017/CBO9781107415324.018>, 2009.
- Negi, H. S., Kokhanovsky, A., and Perovich, D. K.: Application of asymptotic radiative transfer theory for the retrievals of snow parameters using reflection and transmission observations, *The Cryosphere Discussions*, 5, 1239–1262, doi:10.5194/tcd-5-1239-2011, <http://www.the-cryosphere-discuss.net/5/1239/2011/>, 2011.
- Neshyba, S. P., Grenfell, T. C., and Warren, S. G.: Representation of a nonspherical ice particle by a collection of independent spheres for scattering and absorption of radiation: 2. Hexagonal columns and plates, *J. Geophys. Res.*, 108, 4448+, doi:10.1029/2002JD003302, 2003.
- Nicolaus, M., Hudson, S. R., Gerland, S., and Munderloh, K.: A modern concept for autonomous and continuous measurements of spectral albedo and transmittance of sea ice, *Cold Regions Science and Technology*, 62, 14–28, doi:10.1016/j.coldregions.2010.03.001, <http://linkinghub.elsevier.com/retrieve/pii/S0165232X10000406>, 2010.
- Nolin, A. W. and Dozier, J.: A hyperspectral method for remotely sensing the grain size of snow, *Rem. Sens. Environ.*, 74, 207–216, 2000.
- Painter, T. H., Molotch, N. P., Cassidy, M., Flanner, M., and Steffen, K.: Contact spectroscopy for determination of stratigraphy of snow optical grain size, *Journal of Glaciology*, 53, 121–127, doi:10.3189/172756507781833947, <http://dx.doi.org/10.3189/172756507781833947>, 2007.
- Painter, T. H., Rittger, K., McKenzie, C., Slaughter, P., Davis, R. E., and Dozier, J.: Retrieval of subpixel snow covered area, grain size, and albedo from MODIS, *Remote Sensing of Environment*, 113, 868–879, doi:10.1016/j.rse.2009.01.001, <http://linkinghub.elsevier.com/retrieve/pii/S0034425709000029>, 2009.
- Petit, J. R., Jouzel, J., Pourchet, M., and Merlivat, L.: A detailed study of snow accumulation and stable isotope content in Dome C (Antarctica), *Journal of Geophysical Research*, 87, 4301, doi:10.1029/jc087ic06p04301, <http://dx.doi.org/10.1029/JC087iC06p04301>, 1982.
- Picard, G., Arnaud, L., Domine, F., and Fily, M.: Determining snow specific surface area from near-infrared reflectance measurements: Numerical study of the influence of grain shape, *Cold Reg. Sci. Technol.*, 56, 10–17, doi:DOI: 10.1016/j.coldregions.2008.10.001, 2009.
- Picard, G., Domine, F., Krinner, G., Arnaud, L., and Lefebvre, E.: Inhibition of the positive snow-albedo feedback by precipitation in interior Antarctica, *Nature Climate Change*, 2, 795–798, doi:10.1038/nclimate1590, 2012.
- Pirazzini, R., Räisänen, P., Vihma, T., Johansson, M., and Tastula, E.-M.: Measurements and modelling of snow particle size and shortwave infrared albedo over a melting Antarctic ice sheet, *The Cryosphere Discussions*, 9, 3405–3474, doi:10.5194/tcd-9-3405-2015, <http://dx.doi.org/10.5194/tcd-9-3405-2015>, 2015.
- Qu, X. and Hall, A.: What Controls the Strength of Snow-Albedo Feedback?, *J. Climate*, 20, 3971–3981, doi:10.1175/jcli4186.1, <http://dx.doi.org/10.1175/JCLI4186.1>, 2007.



- Ricchiazzi, P., Yang, S., Gautier, C., and Sowle, D.: SBDART: A Research and Teaching Software Tool for Plane-Parallel Radiative Transfer in the Earth's Atmosphere, *Bulletin of the American Meteorological Society*, 79, 2101–2114, doi:10.1175/1520-0477(1998)079<2101:SARATS>2.0.CO;2, <http://journals.ametsoc.org/doi/abs/10.1175/1520-0477%281998%29079%3C2101%3ASARATS%3E2.0.CO%3B2>, 1998.
- 5 Roy, A., Picard, G., Royer, A., Montpetit, B., Dupont, F., Langlois, A., Derksen, C., and Champollion, N.: Brightness temperature simulations of the Canadian seasonal snowpack driven by measurements of the snow specific surface area, *IEEE Trans. Geo. Remote Sensing*, 51, doi:10.1109/TGRS.2012.2235842, <http://ieeexplore.ieee.org/xpl/articleDetails.jsp?arnumber=6476000>, 2013.
- Scambos, T. A., Haran, T. M., Fahnestock, M. A., Painter, T. H., and Bohlander, J.: MODIS-based Mosaic of Antarctica (MOA) data sets: continent-wide surface morphology and snow grain size, *Rem. Sens. Environ.*, 111, 242–257, 2007.
- 10 Schaaf, C. B., Wang, Z., and Strahler, A. H.: Commentary on Wang and Zender—MODIS snow albedo bias at high solar zenith angles relative to theory and to in situ observations in Greenland, *Remote Sensing of Environment*, 115, 1296–1300, doi:10.1016/j.rse.2011.01.002, <http://dx.doi.org/10.1016/j.rse.2011.01.002>, 2011.
- Schaepman-Strub, G., Schaepman, M., Painter, T., Dangel, S., and Martonchik, J.: Reflectance quantities in optical remote sensing—definitions and case studies, *Remote Sensing of Environment*, 103, 27–42, doi:10.1016/j.rse.2006.03.002, <http://dx.doi.org/10.1016/j.rse.2006.03.002>, 2006.
- 15 Stibal, M., Šabacká, M., and Žárský, J.: Biological processes on glacier and ice sheet surfaces, *Nature Geosci*, 5, 771–774, doi:10.1038/ngeo1611, <http://dx.doi.org/10.1038/ngeo1611>, 2012.
- Stroeve, J. C., Box, J. E., and Haran, T.: Evaluation of the MODIS (MOD10A1) daily snow albedo product over the Greenland ice sheet, *Remote Sensing of Environment*, 105, 155–171, doi:10.1016/j.rse.2006.06.009, <http://dx.doi.org/10.1016/j.rse.2006.06.009>, 2006.
- 20 Tanikawa, T., Li, W., Kuchiki, K., Aoki, T., Hori, M., and Stamnes, K.: Retrieval of snow physical parameters by neural networks and optimal estimation: case study for ground-based spectral radiometer system, *Optics Express*, 23, A1442, doi:10.1364/oe.23.0a1442, <http://dx.doi.org/10.1364/OE.23.0A1442>, 2015.
- Tremblin, P., Minier, V., Schneider, N., Durand, G. A., Ashley, M. C. B., Lawrence, J. S., Luong-Van, D. M., Storey, J. W. V., Durand, G. A., Reinert, Y., and et al.: Site testing for submillimetre astronomy at Dome C, Antarctica, *A&A*, 535, A112, doi:10.1051/0004-6361/201117345, <http://dx.doi.org/10.1051/0004-6361/201117345>, 2011.
- 25 Van As, D., van den Broeke, M., and Reijmer, C.: The summer surface energy balance of the high Antarctic plateau, *Boundary-Layer Meteorology*, 115, 289–317, 2005.
- van den Broeke, M., van As, D., Reijmer, C., and van de Wal, R.: Assessing and Improving the Quality of Unattended Radiation Observations in Antarctica, *Journal of Atmospheric and Oceanic Technology*, 21, 1417–1431, doi:10.1175/1520-0426(2004)021<1417:AAITQO>2.0.CO;2, [http://dx.doi.org/10.1175/1520-0426\(2004\)021<1417:AAITQO>2.0.CO;2](http://dx.doi.org/10.1175/1520-0426(2004)021<1417:AAITQO>2.0.CO;2), 2004.
- 30 Wang, X. and Zender, C. S.: MODIS snow albedo bias at high solar zenith angles relative to theory and to in situ observations in Greenland, *Remote Sensing of Environment*, 114, 563–575, doi:10.1016/j.rse.2009.10.014, <http://dx.doi.org/10.1016/j.rse.2009.10.014>, 2010.
- Warren, S. G.: Optical Properties of Snow (Paper 1R1505), *Rev. Geophys. Space Phys.*, 20, 67 — 89, doi:10.1029/RG020i001p00067, 1982.
- Warren, S. G. and Brandt, R. E.: Optical constants of ice from the ultraviolet to the microwave: A revised compilation, *J. Geophys. Res.*, 113, doi:10.1029/2007JD009744, 2008.
- 35 Warren, S. G. and Wiscombe, W. J.: A Model for the Spectral Albedo of Snow. II: Snow Containing Atmospheric Aerosols, *Journal of Atmospheric Sciences*, 37, 2734–2745, doi:10.1175/1520-0469(1980)037, 1980.



Warren, S. G., Brandt, R. E., and O’Rawe Hinton, P.: Effect of surface roughness on bidirectional reflectance of Antarctic snow, *Journal of Geophysical Research*, 103, 25 789, doi:10.1029/98je01898, <http://dx.doi.org/10.1029/98JE01898>, 1998.

Warren, S. G., Brandt, R. E., and Grenfell, T. C.: Visible and near-ultraviolet absorption spectrum of ice from transmission of solar radiation into snow, *Appl. Optic.*, 45, 5320–5334, 2006.

- 5 Zhuravleva, T. B. and Kokhanovsky, A. A.: Influence of surface roughness on the reflective properties of snow, *Journal of Quantitative Spectroscopy and Radiative Transfer*, 112, 1353–1368, doi:10.1016/j.jqsrt.2011.01.004, <http://dx.doi.org/10.1016/j.jqsrt.2011.01.004>, 2011.



12 Octobre 2014



11 November 2014



Figure 1. Picture of the snow surface under Autosolex's head (head 1 is on the left) for two dates 12 October 2014 and 11 November 2014.

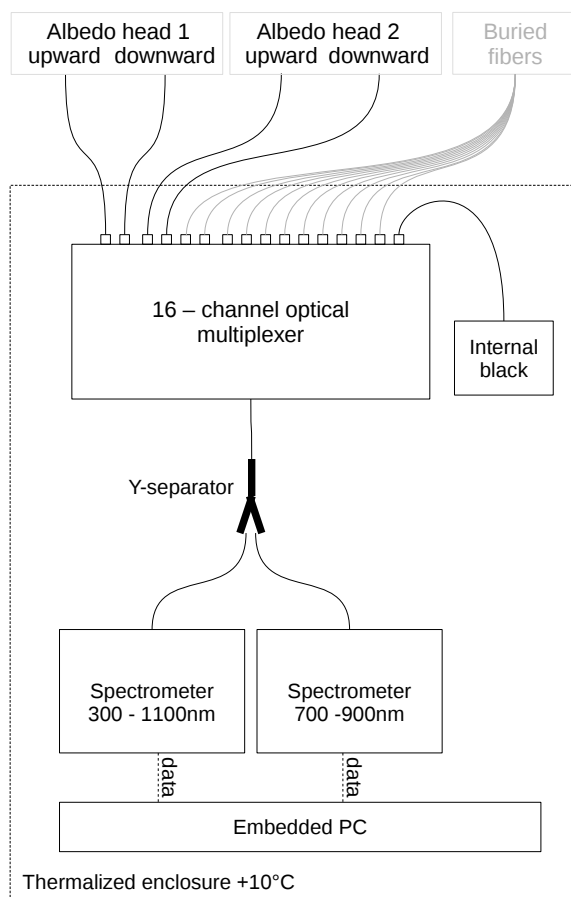


Figure 2. Principle of Autosolex. The dotted rectangle represent the thermalized container that is buried in the snow. The plain curved lines represent fiber optics, the fibers buried in snow (gray) are not used in the present study.

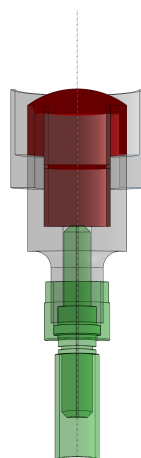


Figure 3. Section of our light collectors. The red parts are in teflon, the remaining is in metal. The tip of the fiber (SMA connector) is shown in green.

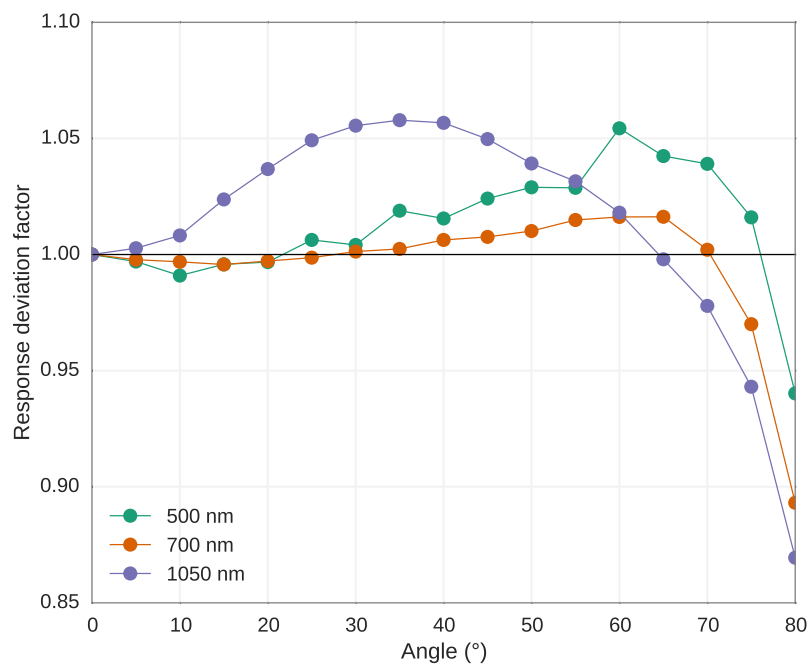


Figure 4. Response of the light collector as a function of the angle for different wavelength. Values are relative to the ideal cosine response.

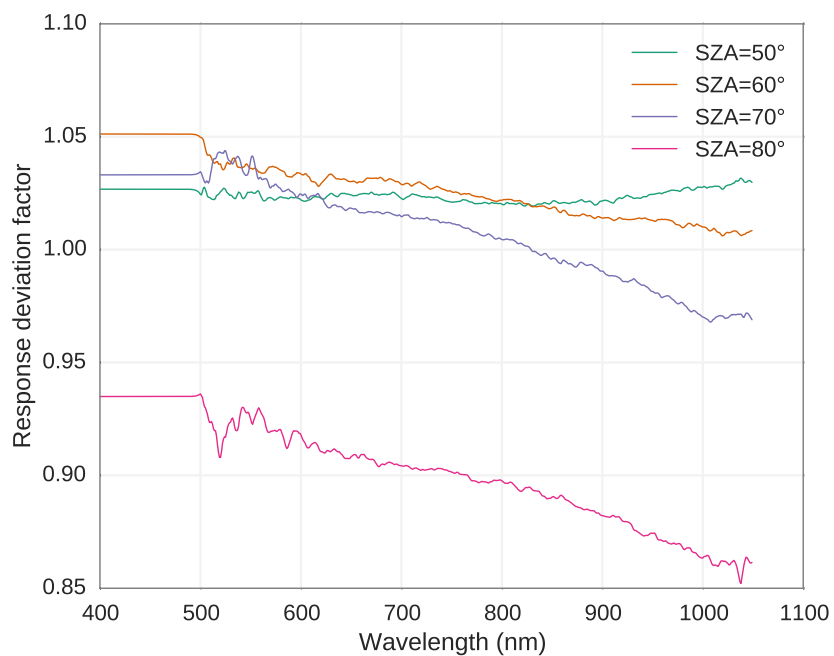


Figure 5. Response of the light collector as a function of the wavelength for different incidence angle. Values are relative to the ideal cosine response.

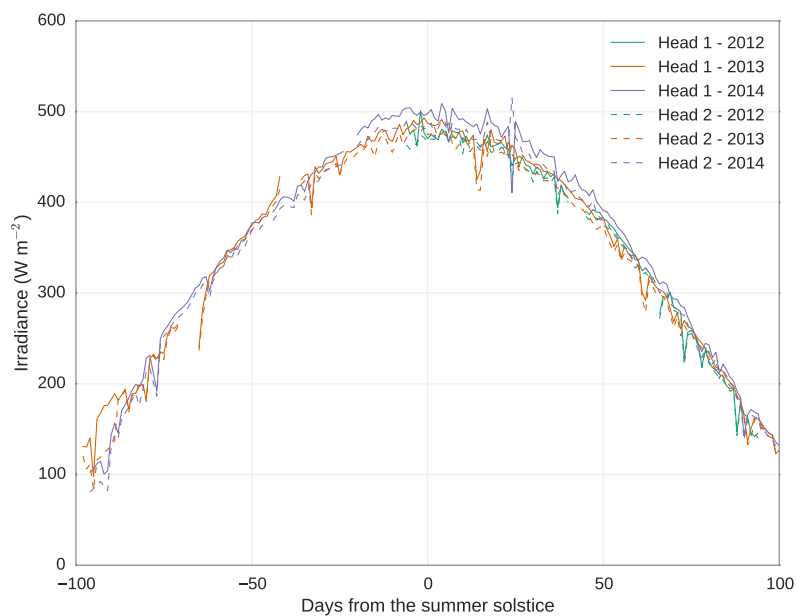


Figure 6. Temporal variations of downwelling irradiance measured by the two heads, averaged every day between 12h and 14h local time, and average between 500 and 600 nm for three summer seasons.

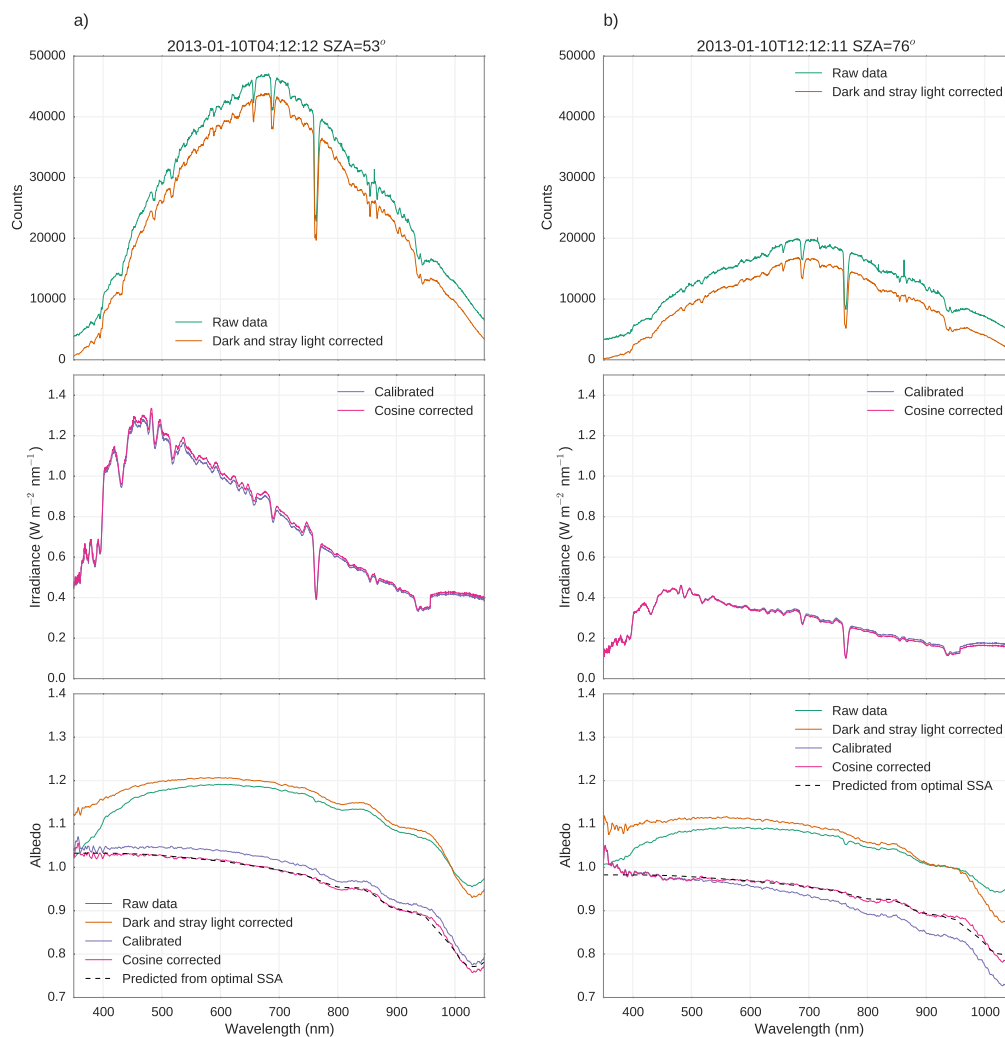


Figure 7. Incident spectrum and albedo at difference stage of the processing for the 10 January 2013, (left) at 12h12 local time and (right) at 20h12 local time. Raw data (green) are first corrected for the dark current and stray light (orange) then calibrated (violet) and last corrected for imperfect collectors (pink). The theoretical spectrum that fits the fully corrected spectrum (pink) is shown in black.

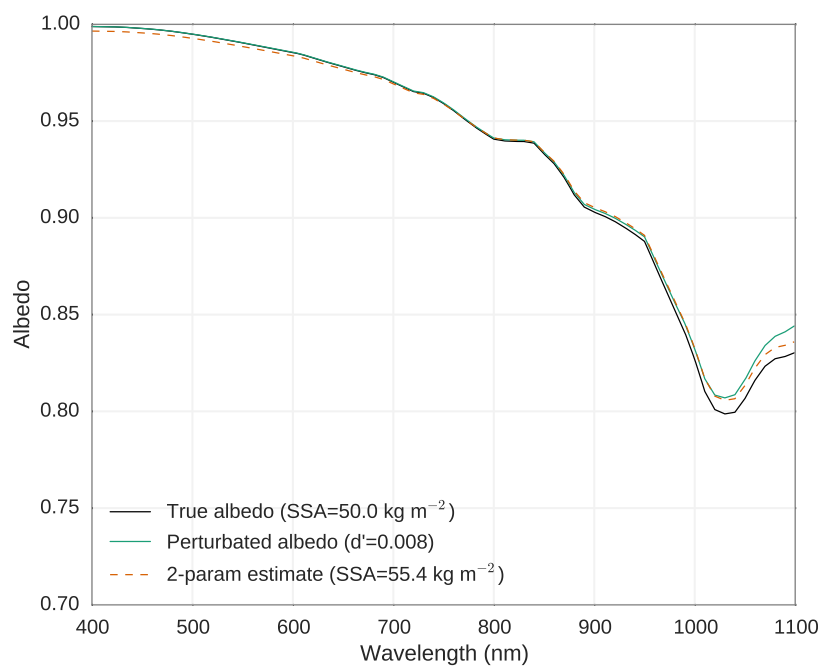


Figure 8. Simulations of albedo spectrum for a SZA=60°. A perfect albedo spectrum for an homogeneous snowpack with SSA of 50 m² kg⁻¹ (black) is perturbed (green) by adding an offset of $d' = 0.8\%$ of the maximum incident irradiance to the incident and reflected irradiance, and used as an observation to estimate SSA. The estimated spectrum is shown in orange, long dash.

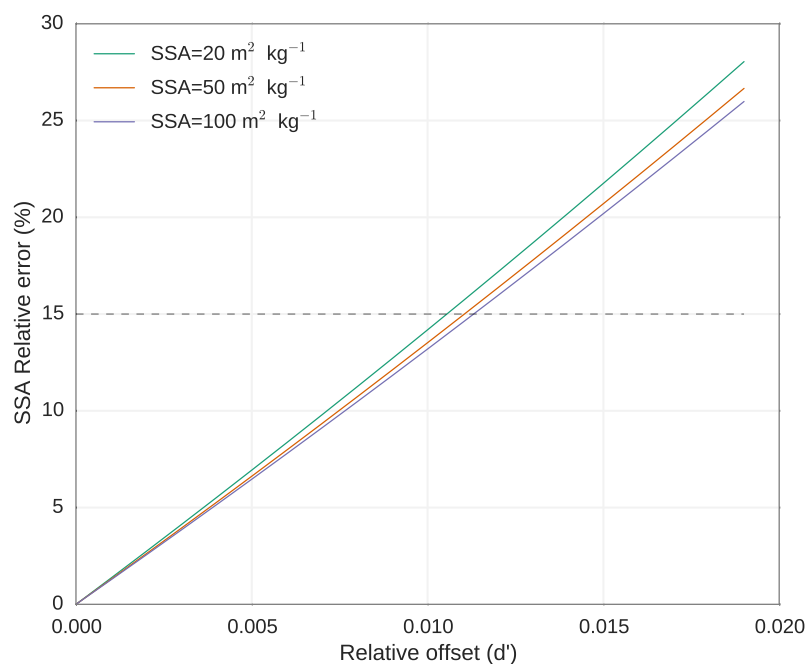


Figure 9. Theoretical calculation of the relative error in SSA due to a spurious offset in the incident and reflectance spectra for SZA=60°. The dashed line shows the 15% target accuracy discussed in the paper.

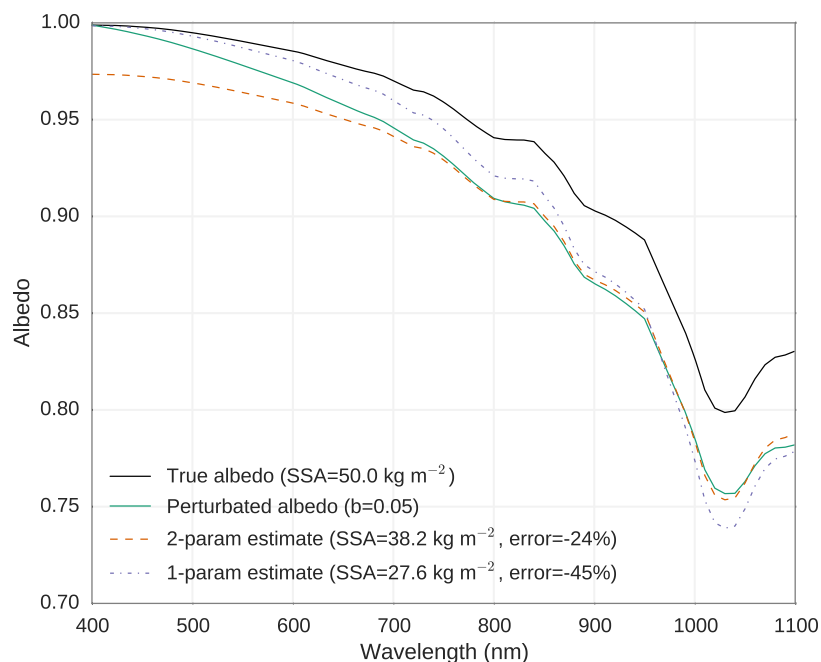


Figure 10. Simulations of albedo spectrum for $SZA=60^\circ$. A perfect albedo spectrum for an homogeneous snowpack with SSA of $50 \text{ m}^2 \text{ kg}^{-1}$ (black) is perturbed by a factor linearly decreasing from 1 at 400 nm to $1 - b$ at 1100 nm with $b = 5\%$ (green) and used as an observation to estimate SSA with the 1-parameter (violet thin dash) and 2-parameter models (orange, long dash). Estimated value are shown in the legend along with the relative error.

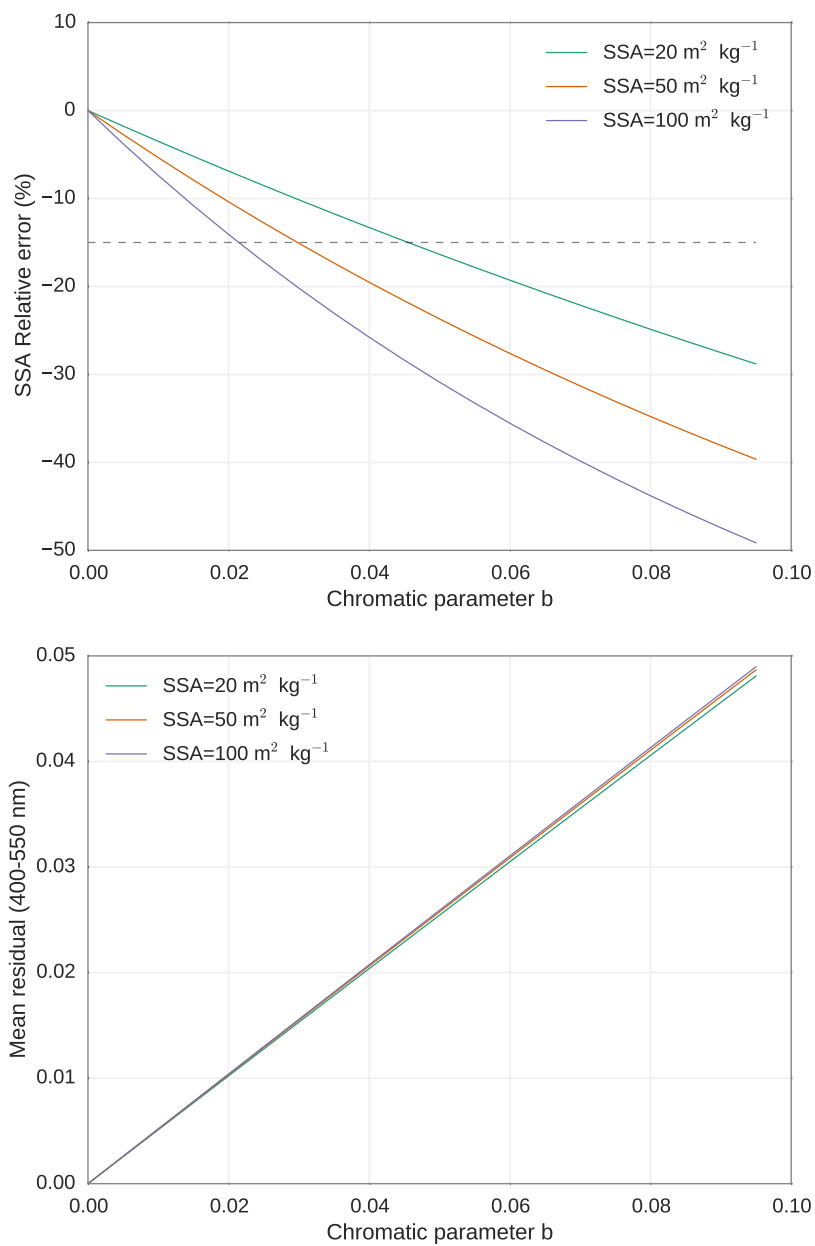


Figure 11. (a) Theoretical calculation of the relative error in SSA due to the chromatic aberration of the spectrometer as a function of the parameter b defined in Equation 14 for $\text{SZA}=60^\circ$. The dashed line shows the 15% target accuracy discussed in the paper. (b) Relationship between b and the residual between the observed and estimate albedo averaged over the range 400 – 550 nm.

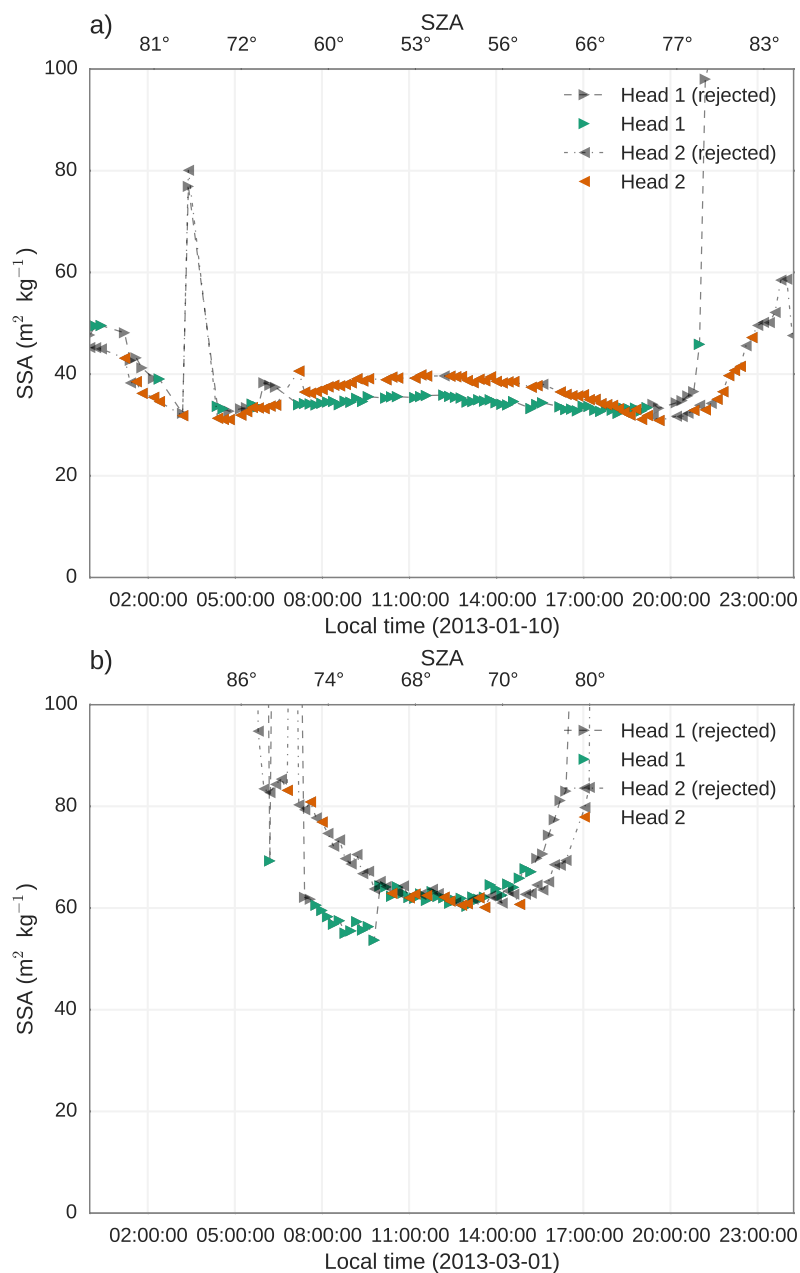


Figure 12. Diurnal variations of estimated SSA for 10 January 2013 (top) and 1st March 2013 (bottom) for the two heads. Gray symbols show data rejected by the quality checks.

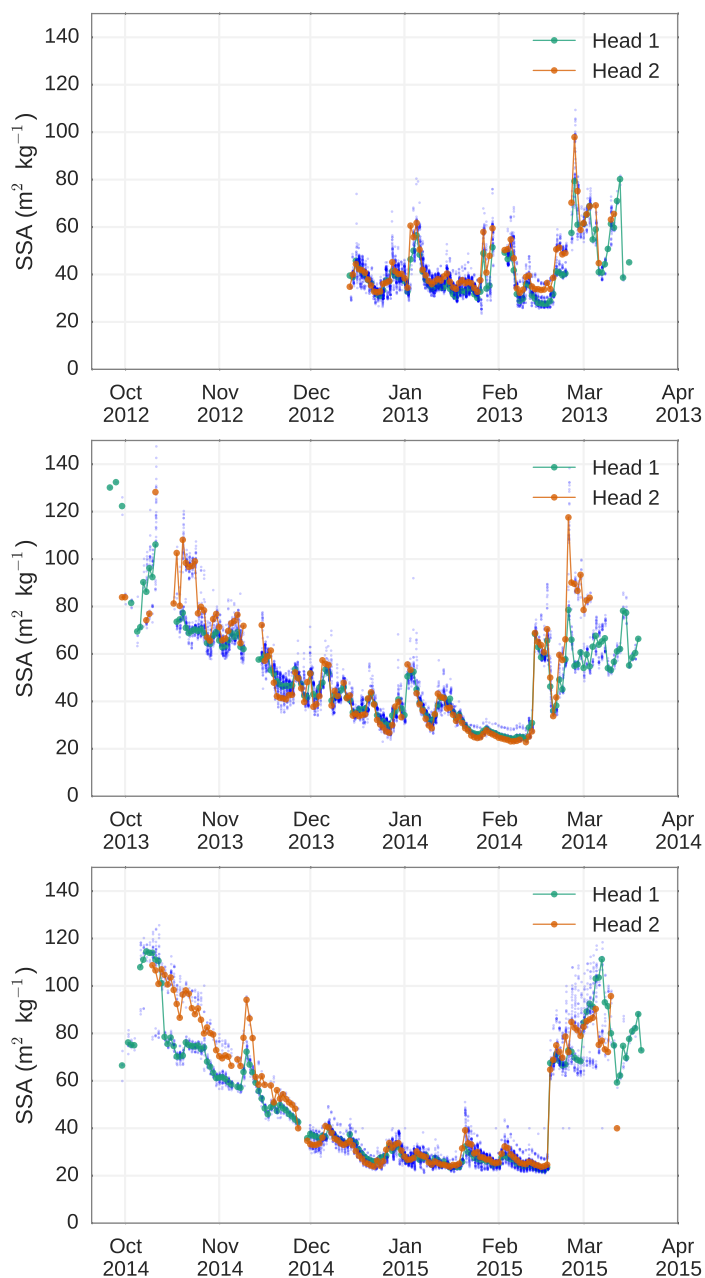


Figure 13. Seasonal variations of SSA for three summers since December 2012 for the two heads. The blue dots show individual valid data (both heads) and the symbols show the daily mean of valid data for each head.

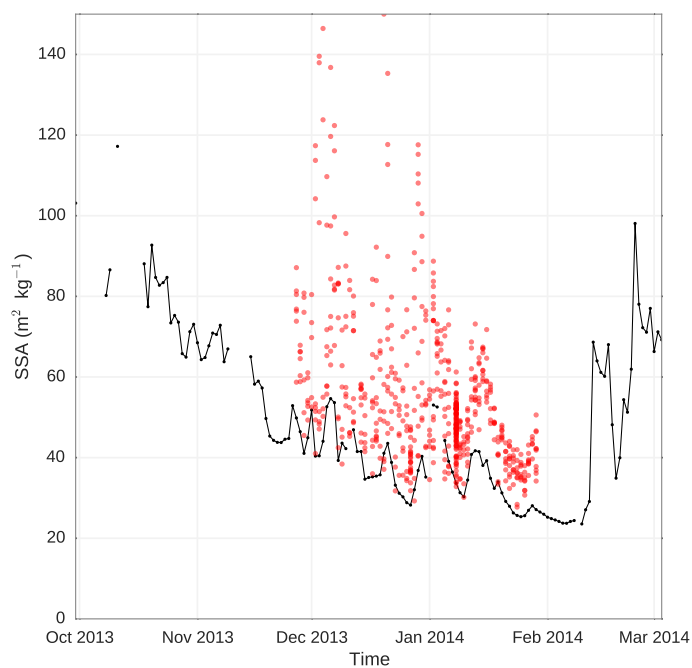


Figure 14. Time-series of daily mean SSA averaged for the two heads of Autosolexs (black line) and manual measurements taken using ASSSAP (red dots).

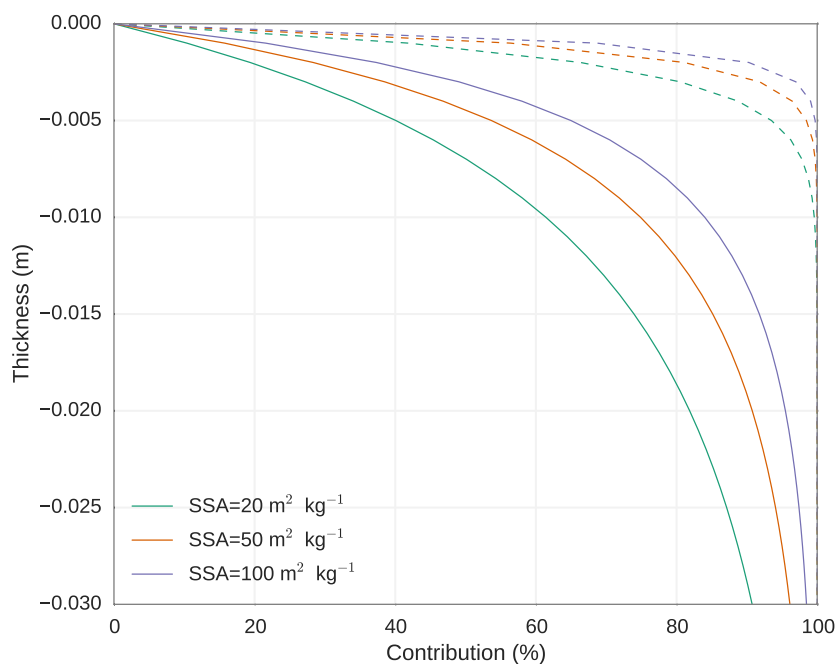


Figure 15. Contribution of the uppermost layer of a semi-infinite snowpack to the albedo averaged over the range 700 – 1050 nm (plain line) and at 1310 nm (dash line) as a function of the layer thickness.